


Article

RBFNN-Based Adaptive Fixed-Time Sliding Mode Tracking Control for Coaxial Hybrid Aerial–Underwater Vehicles Under Multivariant Ocean Disturbances

Mingqing Lu^{1,2,3}, Wei Yang^{2,3}, Zhenyu Xiong^{2,3}, Fei Liao^{2,3,*} , Shichong Wu^{2,3,4}, Yumin Su¹ and Wenhua Wu^{2,3}

¹ National Key Laboratory of Autonomous Marine Vehicle Technology, Harbin Engineering University, Harbin 150001, China; lumingqing@hrbeu.edu.cn (M.L.); suyumin@hrbeu.edu.cn (Y.S.)

² Aerospace Technology Institute, China Aerodynamics Research and Development Center, Mianyang 621000, China; yangwei_cardc@163.com (W.Y.); 18684676361@163.com (Z.X.); wushch5@mail2.sysu.edu.cn (S.W.); academicianWWH@163.com (W.W.)

³ Cross-Domain Flight Cross Technology Laboratory, China Aerodynamics Research and Development Center, Mianyang 621000, China

⁴ School of Systems Science and Engineering, Sun Yat-Sen University, Guangzhou 510275, China

* Correspondence: lfjh1987@mail.usc.edu.cn

Abstract: In this study, the design of an adaptive neural network-based fixed-time control system for a novel coaxial trans-domain hybrid aerial–underwater vehicle (HAUV) is investigated. A radial basis function neural network (RBFNN) approximation strategy-based adaptive fixed-time terminal sliding mode control (AFTSMC) scheme is proposed to solve the problems of the dynamic nonlinearity, model parameter perturbation, and multiple external disturbances of coaxial HAUV trans-media motion. A complete six-degrees-of-freedom model for a continuous water–air cross-domain model is first established based on the hyperbolic tangent transition function, and, subsequently, based on a basic framework of FTSMC, a fixed-time and fast-convergence controller is designed to track the target position and attitude signals. To reduce the dependence of the control scheme on precise model parameters, an RBFNN approximator is integrated into the sliding mode controller for the online model identification of the aggregate uncertainties of the coaxial HAUV, such as nonlinear unmodeled dynamics and external disturbances. At the same time, an adaptive technique is used to approximate the upper bound of the robust switching term gain in the controller, which further offsets the estimation error of the RBFNN and effectively attenuates the chattering effect. Based on Lyapunov stability theory, it is proven that the tracking error can converge in a fixed time. The effectiveness and superiority of the proposed control strategy are verified by several sets of simulation results obtained under typical working conditions.

Keywords: coaxial HAUV; trans-media motion; fixed-time sliding mode control; adaptive technique; RBFNN; online model identification



Citation: Lu, M.; Yang, W.; Xiong, Z.; Liao, F.; Wu, S.; Su, Y.; Wu, W. RBFNN-Based Adaptive Fixed-Time Sliding Mode Tracking Control for Coaxial Hybrid Aerial–Underwater Vehicles Under Multivariant Ocean Disturbances. *Drones* **2024**, *8*, 745. <https://doi.org/10.3390/drones8120745>

Academic Editors: Asiya Khan, Pablo Borja, Dena Bazazian, Daxiong Ji and Mohd Hisham Bin Nordin

Received: 31 October 2024

Revised: 28 November 2024

Accepted: 29 November 2024

Published: 10 December 2024



Copyright: © 2024 by the authors. Licensee MDPI, Basel, Switzerland. This article is an open access article distributed under the terms and conditions of the Creative Commons Attribution (CC BY) license (<https://creativecommons.org/licenses/by/4.0/>).

1. Introduction

Since the Age of Great Navigation, people have come to realize that the ocean covers 71% of the Earth's surface, and there is a huge amount of unexplored area. The vast ocean area is rich in biological resources, renewable resources, mineral resources, and other unexplored energy resources; it has become an important strategic resource affecting the global economy and has attracted increasing attention from all countries. The complex and changeable marine environment has a great impact on the implementation of human production and development activities. With the increasing maturity of modern electronic information technology, various types of marine development and monitoring equipment have emerged, such as marine unmanned aerial vehicles (UAVs) [1], unmanned underwater vehicles (UUVs) [2], unmanned surface vehicles (USVs) [3], and ocean observation buoys (OBs) [4,5], and other types of unmanned equipment have provided great convenience

to researchers. The above-mentioned ocean observation equipment can only perform tasks in a single working medium; however, the increasing demand for multi-domain and cross-domain tasks means that the need for observation equipment capable of carrying out such tasks is becoming increasingly urgent [6]. A type of hybrid aerial–underwater vehicles (HAUVs) with a water–air amphibious operation capability has emerged. The unique multi-media maneuverability of HAUVs gives them strong potential for military and civil applications [7], and it has attracted extensive attention from scholars in recent years. Researchers from various countries have conducted active research on HAUVs and obtained fruitful research results [8,9].

The idea of combining a submarine and an aircraft appeared in the science novel *Master of the World* by Jules Verne in 1904 [10]. By 1934, the Soviet Union had begun the development of a manned HAUV program, codenamed LPL [11,12]. This was followed by the development of the RFS-1 [13] and CONVAIR [14] prototypes. Since then, aeronautical design experience has been applied to the study of HAUVs, and, as a result, HAUV configurations have been designed using conventional structures such as fixed-wing, multi-rotor, and flapping-wing configurations. Meanwhile, there is also a composite wing structure scheme combining fixed-wing and multi-rotor structure designs, as well as combining vertical takeoff and landing (VTOL) capabilities with the characteristic of long endurance [6–9]. However, the complex structure design and weight of the power system are great challenges for this HAUV design. For bionic-designed HAUVs, the typical cross-domain modes are flapping wings [15], squirting water, or jets [16,17]. This short and intense cross-domain maneuvering strategy also leads to the threat of water lapping against the structure of the body. This short and rapid jump action brings great challenges in terms of controller design [18]. Multi-rotor HAUVs based on closed-loop feedback control and with VTOL capabilities have won the favor of a great number of researchers for their significant advantages in flexibility and control stability, and researchers have achieved significant research results [19,20].

With a variety of prototypes being developed, HAUV controller designs have emerged in recent years. The classical proportion differentiation/proportion integration differentiation (PD/PID) linear control strategy has been widely used in previous studies due to its simple structure and convenient engineering application [21–24]. To further improve the working characteristics of classical linear controllers, an improved PID control strategy is gradually being derived. Active disturbance rejection control (ADRC)-based strategies [25] and Fuzzy P+ID [26] have also been applied to HAUV systems. In addition, [27] proposed an improved PID controller that combines an intelligent genetic algorithm (GA) and a radial basis function neural network (RBFNN) to address the height control problem of cross-domain processes. The limitation of the poor robustness of linear controllers cannot be completely overcome by the above improvement; thus, with the progress of control technology, the nonlinear control strategy has come to be widely used in HAUV control. In particular, sliding mode control (SMC) is widely used in the controller design of various robot systems due to its insensitivity to model perturbation and strong robustness to external interference [28]. In the literature [29], a classic SMC controller was designed for a tilt HAUV, and the effectiveness of this method was verified in terms of altitude and attitude control. Ma et al. developed an adaptive sliding mode control (ASMC) strategy for double-layer HAUVs [30]. Bi et al. modeled and analyzed the cross-media process of Nezha series HAUVs and designed a second-order SMC controller [31]. To improve the response speed of the HAUV control system, the authors also designed an adaptive finite-time fast terminal sliding mode controller (AFTSMC) for coaxial HAUVs in their previous work [32]. Many scholars have also attempted to develop other nonlinear controllers, such as an adaptive dynamic surface control (ADSC) strategy [33], a dynamic surface architecture combined with a nonlinear disturbance observer (NDO) scheme [34], nonlinear dynamic inverse (NDI) [35], and an MPC-SMC cascade controller [36]. Many of the above works have carried out effective explorations of cross-media movement, but, in

practice, cross-domain movement control strategies still face many unknown difficulties and challenges [18].

The above-mentioned controller settlement time involved in HAUV cross-domain control depends on the initial state. In the actual process of crossing the water–air interface, the time window for the operation of cross-media motion is very short, and a controller stability time that is too long may lead to the failure of the cross-domain maneuver. Therefore, the idea of finite-time control is introduced into the controller design for HAUVs [32]. In the literature [37], a finite-time controller based on a backstepping framework was designed and approached the unknown hydrodynamic parameters by integrating a reinforcement learning neural network. With more stringent requirements on system reaction time, the finite-time control method was further developed into fixed-time control, which, to date, has been widely adopted in mature equipment such as spacecraft, UAVs, and AUVs [38,39]. Based on the above literature research and encouragement, it is a good choice to use the design framework of a fixed-time sliding mode controller to solve cross-medium maneuvering control under multiple interference conditions. However, a basic SMC controller is designed by assuming that the exact model parameters of the HAUV system are known, excluding the dynamic characteristics of the model, complex hydrodynamic effects, etc. [40]. The existing SMC methods usually design an adaptive law to approximate the gain of the discontinuous control part to enhance the robustness of the system [41], while the compound uncertainty caused by environmental disturbance and model parameter perturbation in the cross-domain process may lead to system chattering due to the overestimation of parameters. The radial basis function neural network (RBFNN) is one of the most popular intelligent computing methods; it has a strong online learning ability and can realize the approximation of nonlinear continuous functions with arbitrary precision [42]. To date, control based on neural networks has been widely used in the trajectory tracking control of robot systems [43]. The RBFNN approximator is used to estimate and compensate for the lumped uncertainties caused by the complex hydrodynamic characteristics and time-varying parameters of HAUVs in cross-domain maneuvering, and the adaptive technique is introduced to further offset the residual estimation error. The combined action of the RBFNN and adaptive law further improves the stability and robustness of the system. Based on the above research scheme, a neural network-based adaptive fixed-time terminal sliding mode controller (NNAFTSMC) is designed and applied to the cross-domain maneuvering control of coaxial HAUVs facing multiple complex ocean disturbances and parameter uncertainty.

Inspired by previous research results, the main advantages of the control algorithm designed in this study can be summarized as follows:

- (1) The external force of the whole trans-media process is analyzed in detail. A continuous approximation function based on the hyperbolic tangent function is introduced into the dynamic model to establish a continuous dynamic model, which avoids the instability caused by a sudden change in model parameters.
- (2) Compared with the existing HAUV control strategy, the fixed-time control idea ensures that the trajectory tracking error converges within a predetermined time and improves the response speed of the control system.
- (3) An adaptive sliding mode controller based on the RBFNN approximator is designed. On the one hand, the nonlinear model and hydrodynamic term of coaxial HAUVs are identified online using the RBFNN approximator. On the other hand, by combining the adaptive algorithm, the composite robustness of the system is improved, and the inherent chattering phenomenon of SMC is effectively weakened.

The remainder of this paper is organized as follows: In Section 2, the workflow of a coaxial HAUV prototype is given, and the kinematics and dynamics of the system are modeled. In Section 3, the design process of an adaptive fixed-time sliding mode controller using an RBFNN to approximate the nonlinear part of the coaxial HAUV is detailed, and the fixed-time stability of the system is demonstrated using the Lyapunov stability theory. The stability and fastness of the proposed method are verified in simulations, and the

simulation results are compared and analyzed in Section 4. The conclusions and outlooks for future work are given in Section 5.

2. Dynamics Modeling of a Coaxial HAUV

2.1. Coaxial HAUV Overview

A novel coaxial HAUV system is proposed, as shown in Figure 1. This coaxial HAUV can pass smoothly between air and water, and it can be operated from a support ship or deployed by aircraft. The HAUV is designed to operate in two main modes. When it is equipped with an auxiliary float, it can assume the role of a drifting buoy; at this time, it has enough buoyancy to float freely without additional energy consumption to maintain the floating state, and it can also carry out dynamic positioning on the water surface to perform the task of formation array. When the float is discarded, the HAUV is in a negative buoyancy state; at this time, it can dive underwater and perform underwater maneuvering through the power system, perform underwater sampling and underwater maneuvering tasks, and, when necessary, repeatedly perform cross-media operations requiring entry into and exit out of the water.

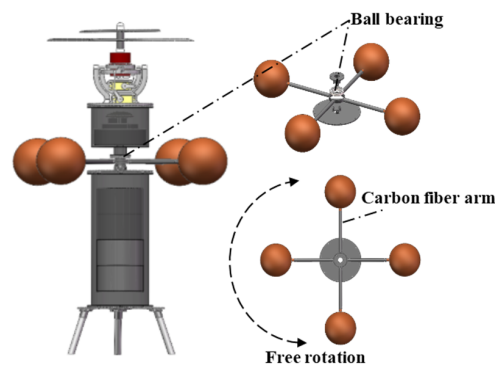


Figure 1. Structure diagram of coaxial HAUV.

Figure 2 shows the most typical working state of a coaxial HAUV, that is, the full-flow cross-domain maneuver operation process. When the coaxial HAUV needs to return for recovery, it first rises from the water using the propeller, leaves the water and enters the air, and then quickly returns to land on the oceanographic survey ship or changes the mission area to perform landing operations and re-enters the water to perform the mission. Coaxial HAUVs can carry different measuring devices to perform multiple tasks, and, when multiple coaxial HAUVs work together, they can maintain measurement formations to ensure measurement accuracy.

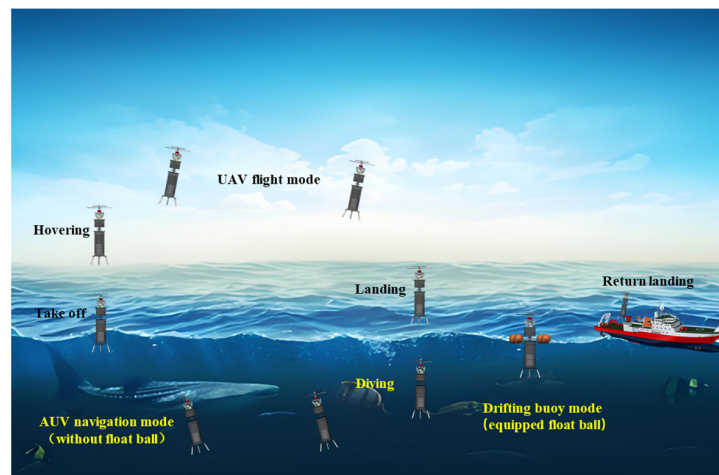


Figure 2. Flowchart of deployment and operation of coaxial HAUV.

2.2. Pre-Preparation

In order to facilitate further dynamics model analysis and controller design, some useful assumptions, definitions, notations, and lemmas are presented here.

Notation [44]. In this paper, for vector $\mathbf{x} = [x_1, x_2, \dots, x_n]^T$, $\|\mathbf{x}\|$ denotes the Euclidean or 2-norm of \mathbf{x} , $|\mathbf{x}|^r = [|x_1|^r, |x_2|^r, \dots, |x_n|^r]^T$, $\text{sig}^r(\mathbf{x}) = [\text{sig}^r(x_1), \text{sig}^r(x_2), \dots, \text{sig}^r(x_n)]^T$, $\text{sig}^r(x_i) = |x_i|^r \text{sign}(x_i)$, where $\text{sign}(\cdot)$ is a signum function, and r represents the scalar constant.

Lemma 1 [45]. For any bounded initial state $\mathbf{x}(0)$, if there exists a continuous positive definite Lyapunov function $V(\mathbf{x})$ satisfying the condition.

$$\begin{aligned} \dot{V}(\mathbf{x}) &= -\alpha V(\mathbf{x}) + \beta \\ k_1 \|\mathbf{x}\| &\leq V(\mathbf{x}) \leq k_2 \|\mathbf{x}\| \end{aligned} \quad (1)$$

where $k_1, k_2: \mathbb{R}^n \rightarrow \mathbb{R}$ are class κ functions, and $\alpha > 0, \beta > 0$ are positive constants, then $\mathbf{x}(t)$ is semi-globally uniformly terminally bounded, and $\mathbf{x}(t)$ achieves asymptotic stability.

Lemma 2 [46]. Consider the existence of the following nonlinear continuous system: $\dot{\mathbf{x}} = f(\mathbf{x}), \mathbf{x}(0) = 0, f(0) = 0, \mathbf{x} \in \mathbb{R}^n$. If there is a positively definite Lyapunov function $V(\mathbf{x})$ that satisfies the relation

$$\dot{V}(\mathbf{x}) = -\alpha V(\mathbf{x})^{\frac{m}{n}} - \beta V(\mathbf{x})^{\frac{p}{q}} + \Delta \quad (2)$$

where $\alpha > 0, \beta > 0, 0 < \Delta < +\infty$, and m, n, p, q are positive odd numbers that satisfy $m < n$ and $p > q$, then, the system is practically fixed-time stable, and $V(\mathbf{x})$ will converge to the following compact set in fixed time:

$$\Omega = \left\{ V(\mathbf{x}) \in \mathbb{R} \mid V(\mathbf{x}) \leq \min \left\{ \left(\frac{\Delta}{\alpha(1-\iota)} \right)^{\frac{n}{m}}, \left(\frac{\Delta}{\beta(1-\iota)} \right)^{\frac{q}{p}} \right\} \right\} \quad (3)$$

where $0 < \iota < 1$, and the convergence time T is approximated using $T \leq T_{max} = \frac{1}{\alpha(1-m/n)} + \frac{1}{\beta(p/q-1)}$.

Lemma 3 [47]. If it exists, a scalar system takes the following form:

$$\dot{y} = -\alpha y^{l_1} - \beta y^{l_2} \quad (4)$$

where $\alpha > 0, \beta > 0, 0 < l_1 < 1$, and $1 < l_2$. Then, system (4) is fixed-time stable, and the convergence time is approximated using the following equation:

$$T \leq T_{max} = \frac{1}{l_1(1-l_1)} + \frac{1}{l_2(l_2-1)} \quad (5)$$

Lemma 4 [48]. For any constant $\chi > 0$, the following inequality holds:

$$|x| \leq \chi \tanh\left(\frac{x}{\chi}\right) + \chi \kappa \quad (6)$$

where $\kappa = 0.2785$.

Lemma 5 [49]. The form of the RBFNN-based online approximator is as follows: for any nonlinear continuous function $f(\mathbf{x})$, there exists a vector of ideal weights \mathbf{W} such that the function is approximated in the following form:

$$f(\mathbf{x}) = \mathbf{W}^T \mathbf{h}(\mathbf{x}) + \varepsilon, 0 < |\varepsilon| \leq \bar{\varepsilon} \quad (7)$$

where $\mathbf{W} = [W_1, W_2, \dots, W_m]^T$ and $\mathbf{x} = [x_1, x_2, \dots, x_n]^T$ are the weight and input vectors; m and n indicate the numbers of nodes and inputs; ε and $\bar{\varepsilon}$ denote the estimation error (ε is sufficiently small under the condition of the ideal weight parameter) and its upper bound; and $\mathbf{h}(\mathbf{x}) = [h_1(\mathbf{x}), h_2(\mathbf{x}), \dots, h_m(\mathbf{x})]^T$ is a Gaussian basis function vector defined as follows:

$$h_i(\mathbf{x}) = \exp\left(-\frac{\|\mathbf{x} - \mathbf{c}_i\|^2}{2b_i^2}\right), i = 1, \dots, p \tag{8}$$

where \mathbf{c}_i is the i th center vector, and b_i is the width value of the i th neural network Gaussian basis function, which is used to control the smoothness of the interpolation function. In this type of basis function, the closer the input is to the center, the larger the output value obtained.

Linear combinations of Gaussian functions can be used to approximate any continuous nonlinear function with arbitrary precision. In addition, neurons with Gaussian basis functions have a selective response; that is, they have a high activation characteristic for inputs close to the center of the neuron and a low activation characteristic for inputs far from the neuron. This characteristic reduces the amount of computation and improves the learning rate of the neural network. Therefore, the RBFNN chooses the Gaussian function as the basic function.

The neural ideal weight network's ideal weight \mathbf{W} is unknown and needs to be estimated. By setting $\hat{\mathbf{W}}$ as the estimate of the ideal weight of the neural network, we can obtain an estimate of $\hat{f}(\mathbf{x})$:

$$\hat{f}(\mathbf{x}) = \hat{\mathbf{W}}^T \mathbf{h}(\mathbf{x}) \tag{9}$$

In the literature, extensive research has found that, if accurate approximation values of weight parameters are obtained, then nonlinear functions can be approximated with a minimum error. The above is the action mechanism of the universal approximation of the RBFNN approximator.

Assumption 1. *The mass of the coaxial HAUV is uniformly distributed on a cylindrical, watertight body structure, which is symmetric with respect to the three coordinate planes. Violent maneuvering is not considered during trans-media maneuvering, and the complex coupled hydrodynamic coefficients and higher-order hydrodynamic coefficients are neglected.*

2.3. Multimodal Dynamics Modeling

In this section, a dynamic model of the coaxial HAUV is established. The coaxial HAUV has a coaxial rotor structure mounted on a vector platform, and horizontal motion is achieved by adjusting the coupled pitch and roll angle, which is realized by tilting the vector platform to change the direction of the vector thrust. The whole system has only four inputs: the thrust generated by the two rotors and the triaxial directional torque generated by the vector platform and the rotors. It can be seen that the coaxial HAUV is a typical underdriven highly coupled system.

The HAUV is generally regarded as a rigid body when establishing the coordinate system, and the kinetic equations are established based on rigid body dynamics and kinematics. As shown in Figure 3, the inertial coordinate system is $R_E\{o_e x_e y_e z_e\}$, and the body-fixed coordinate system is $R_B\{o_b x_b y_b z_b\}$. The origin of R_B is set at the center of gravity of the HAUV body. The position and attitude vectors in the coordinate system R_E are denoted by $\boldsymbol{\eta}_1 = [x \ y \ z]^T$ and $\boldsymbol{\eta}_2 = [\phi \ \theta \ \psi]^T$. $\mathbf{v}_1 = [u \ v \ w]^T$ and $\mathbf{v}_2 = [p \ q \ r]^T$ are the linear and angular velocity vectors in the coordinate system R_B .

$$\mathbf{J}_1 = \begin{bmatrix} c\theta c\psi & s\phi s\theta c\psi - c\phi s\psi & c\phi s\theta c\psi + s\phi s\psi \\ c\theta s\psi & s\phi s\theta s\psi + c\phi c\psi & c\phi s\theta s\psi - s\phi c\psi \\ -s\theta & s\phi c\theta & c\phi c\theta \end{bmatrix}, \mathbf{J}_2 = \begin{bmatrix} 1 & s\phi t\theta & c\phi t\theta \\ 0 & c\phi & -s\phi \\ 0 & s\phi/c\theta & c\phi/c\theta \end{bmatrix} \tag{10}$$

$$J = \begin{bmatrix} J_1 & \mathbf{0}_{3 \times 3} \\ \mathbf{0}_{3 \times 3} & J_2 \end{bmatrix} \quad (11)$$

where, $s(\cdot)$, $c(\cdot)$, and $t(\cdot)$ denote the sine, cosine, and tangent functions, respectively. J is the transformation matrix. J_1 is the transformation matrix of the position loop and J_1 is an orthogonal matrix, so it satisfies $J_1^{-1} = J_1^T$. J_2 is the transformation matrix of the attitude loop. Thus, the kinematic equations of the HAUV can be written as follows [50]:

$$\begin{cases} \dot{\eta} = Jv \\ M\dot{v} + C_v v + D_v v + g_v = \tau_v + \tau_{dv} \end{cases} \quad (12)$$

where $M = M_{RB} + M_A$ is the mass (in physics) matrix; $C = C_{RB} + C_A$ is the Coriolis force matrix; $D_v = D_{va} + D_{vw}$ is the damping matrix; g_v is the restoring force matrix, including gravity and buoyancy; τ_v is the control force matrix; and τ_{dv} is the generalized uncertainty matrix.

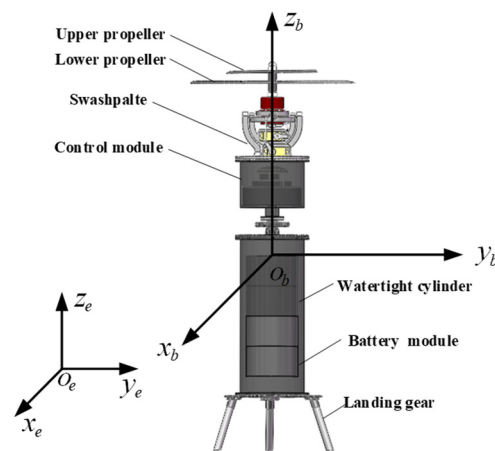


Figure 3. Main outline drawing and coordinate system of coaxial HAUV.

2.3.1. Description of Transition-State Switching Trans-Media

Define a switching function k . The switching coefficient is appended to the hydrodynamic parameters as a product factor to make the hydrodynamic parameters change with the switching coefficient. $k = 1$ indicates that the HAUV is in an underwater state. The hydrodynamic effect is 1. In this case, the body is only subject to hydrodynamic action. $k = 0$ indicates that the HAUV is in a flying-in-air state. This means that the HAUV body is completely exposed to the air and is only affected by aerodynamic action. $k_s \in (0, 1)$ means that the HAUV body is partially submerged in water and partially exposed to air and thus subjected to a combination of hydrodynamic and aerodynamic action.

The changing trend of the additional variables is characterized by setting the switching coefficient, which links the processes of the HAUV’s underwater and air maneuvers. The existing switching coefficients mainly have step forms k_{sign} and linearized forms k_{lin} [51]. The two switching functions are discontinuous, which can easily cause the model to mutate and make the controller unstable. Inspired by continuous sliding mode control, a switching function based on the hyperbolic tangent function k_{tanh} is introduced into the dynamic model to make the transition smoother while satisfying the model variation accuracy as much as possible.

$$\begin{aligned} k_{step} &= 1/2(1 - \text{sign}(z)) \\ k_{lin} &= \begin{cases} 0, z \geq h/2 \\ 1/2(1 - 2z/h), -h/2 < z < h/2 \\ 1, z \leq -h/2 \end{cases} \\ k_{tanh} &= 1/2(1 - \tanh(z/\mu)) \end{aligned} \quad (13)$$

Here, h is the altitude of the coaxial HAUV; z is the altitude of motion in the inertial coordinate system of the vehicle; and $0 < \mu < 0$ is the parameter to be designed, which can adjust the slope of the transition coefficient. Let $k_s = k_{\tanh}$ represent the approximate pattern of the hydrodynamic change in the coaxial HAUV; $k_{sa} = 1 - k_s$ indicates the switching coefficient of the air resistance coefficient, which describes the trend of influencing factors in the air. Obviously, the trend of dynamics in the air is the opposite of that of the hydrodynamic change process. Figure 4 shows the variation trend of different switching coefficients with height.

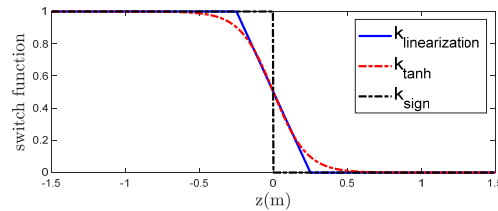


Figure 4. Three types of switching coefficients.

Next, the cross-media dynamic evolution process of the parameters and variables in the model (12) is analyzed.

2.3.2. Added Mass

Considering the approximate symmetry of the HAUV, the mass matrix and the moment of inertia matrix are both principal diagonal matrices and can be expressed as follows [29]:

$$M = M_{RB} + M_A \tag{14}$$

where $M = M_{RB} + M_A$ is the mass matrix; $M_{RB} = \text{diag}(m, m, m, I_x, I_y, I_z)$ and M_A are the nominal (when drying the body) mass matrix and the additional mass matrix, respectively. The coaxial HAUV carries some of the water near its body with it during underwater maneuvering, which is the cause of additional mass. The additional mass matrix can be approximated in the form of a principal diagonal matrix $M_A = -k_s \text{diag}(X_{\dot{u}}, Y_{\dot{v}}, Z_{\dot{w}}, K_{\dot{p}}, M_{\dot{q}}, N_{\dot{r}})$.

M is a diagonal matrix, which can be expressed as a partitioned matrix: $M = \begin{bmatrix} M_{11} & \mathbf{0}_{3 \times 3} \\ \mathbf{0}_{3 \times 3} & M_{22} \end{bmatrix}$.

2.3.3. Coriolis and Centripetal Forces

The Coriolis force comes from the inertia of an object’s motion. From the definition of the Coriolis force, it can be seen that this is an inherent property of moving objects. However, as the parameters of the physical model in the trans-media process of the coaxial HAUV are time-varying, the Coriolis force is also time-varying, which can be expressed as follows [37]:

$$C_v = C_{RB} + C_A \tag{15}$$

$$C_{RB} = \begin{bmatrix} 0 & 0 & 0 & 0 & mw & -mv \\ 0 & 0 & 0 & -mw & 0 & mu \\ 0 & 0 & 0 & mv & -mu & 0 \\ 0 & mw & -mv & 0 & I_z r & -I_y q \\ -mw & 0 & mu & -I_z r & 0 & I_x p \\ mv & -mu & 0 & I_y q & -I_x p & 0 \end{bmatrix} \tag{16}$$

$$C_A = \begin{bmatrix} 0 & 0 & 0 & 0 & -Z_{\dot{w}W} & Y_{\dot{v}V} \\ 0 & 0 & 0 & Z_{\dot{w}W} & 0 & -X_{\dot{u}U} \\ 0 & 0 & 0 & -Y_{\dot{v}V} & X_{\dot{u}U} & 0 \\ 0 & -Z_{\dot{w}W} & Y_{\dot{v}V} & 0 & -N_{\dot{r}r} & M_{\dot{q}q} \\ Z_{\dot{w}W} & 0 & -X_{\dot{u}U} & N_{\dot{r}r} & 0 & -K_{\dot{p}p} \\ -Y_{\dot{v}V} & X_{\dot{u}U} & 0 & -M_{\dot{q}q} & K_{\dot{p}p} & 0 \end{bmatrix}$$

where C_v represents the Coriolis force matrices, and C_{RB} and C_A are the nominal and additional Coriolis force matrices, respectively. Obviously, the matrix C_A is related to the additional mass of the coaxial HAUV and the current motion state, and, when the added mass disappears, C_A also returns to 0.

2.3.4. Resistance and Resistance Moment

As the density of water is much higher than that of air, the drag effect of vehicles driving in water is very significant. Coaxial HAUVs are also affected by drag moments when they change their attitude in water. It is generally accepted that the drag force and drag moment are proportional to the square of the linear and angular velocities of the underwater motion [34].

$$\begin{bmatrix} f_d \\ \tau_d \end{bmatrix} = -D_v(v_1, v_2) \begin{bmatrix} v_1 \\ v_2 \end{bmatrix} \tag{17}$$

$$\begin{aligned} D_v &= D_w + D_a \\ &= k_s \text{diag} \left(X_{u|u}|u|, Y_{v|v}|v|, Z_{w|w}|w|, K_{p|p}|p|, M_{q|q}|q|, N_{r|r}|r| \right) \\ &\quad + k_{sa} \text{diag} \left(X_{u|u|a}|u|, Y_{v|v|a}|v|, Z_{w|w|a}|w|, K_{p|p|a}|p|, M_{q|q|a}|q|, N_{r|r|a}|r| \right) \end{aligned} \tag{18}$$

Here, D_w and D_a are the damping coefficient matrices of the coaxial HAUV in water and air, respectively, and D is the combined damping coefficient.

2.3.5. Restoring Force and Restoring Moment

In the inertial coordinate system, the direction of gravity of the coaxial HAUV in water is opposite to the positive direction of the z_e -axis, but the direction of buoyancy is the same as the positive direction of the z_e -axis. The magnitude of the buoyancy force is obtained from Archimedes' principle, and, as the origin of the body-fixed coordinate system coincides with the center of gravity of the coaxial HAUV, gravity does not produce torque. The effects of gravity and buoyancy on the coaxial HAUV are expressed as follows [31]:

$$\begin{aligned} f_g &= -mg J_1^T [0 \ 0 \ 1]^T \\ &= -mg [-\sin \theta \ \sin \phi \cos \theta \ \cos \phi \cos \theta]^T \\ \tau_g &= [0 \ 0 \ 0]^T \end{aligned} \tag{19}$$

$$\begin{aligned} f_b &= k_s \rho_w V g J_1^T [0 \ 0 \ 1]^T \\ &= k_s \rho_w V g [-\sin \theta \ \sin \phi \cos \theta \ \cos \phi \cos \theta]^T \\ \tau_b &= r_b \times f_b \end{aligned} \tag{20}$$

where ρ_w is the density of water, V is the volume of the HAUV's watertight chamber, and g is the acceleration of gravity. The center of the buoyancy coordinates is defined as $r_b = [x_b \ y_b \ z_b]^T$. Based on the above analysis, the restoring force is expressed as a vector:

$$g_v = - \begin{bmatrix} f_g + f_b \\ \tau_g + \tau_b \end{bmatrix} \tag{21}$$

Remark 1. It is worth noting that, according to the basic ship principle, the stability of a floating body is closely related to the height of the initial metacenter, and the position of the center of buoyancy is dynamic during the cross-domain process of the coaxial HAUV, which makes the recovery moment difficult to quantify. The special elongated structure of the coaxial HAUV causes a minimal change in the horizontal position of the center of buoyancy during its trans-domain motion. The simplified

rule of change in the position of the center of action of the wind force and the center of buoyancy is given here.

$$z_b = \begin{cases} 0, z > h/2 \\ k_s z_{b0} - (h/2 + z)/2, -h/2 \leq z \leq h/2 \\ z_{b0}, z < -h/2 \end{cases} \tag{22}$$

$$z_w = \begin{cases} 0, z > h/2 \\ h/2 - (h/2 + z)/2, -h/2 \leq z \leq h/2 \\ 0, z < -h/2 \end{cases} \tag{23}$$

Here, z_{b0} is the vertical coordinate value of the center of gravity in the body-fixed coordinate system under fully submerged conditions.

The position of the center of action of the wind force and the center of buoyancy in the body coordinate system can be approximated using mathematical calculations.

$$\begin{aligned} \mathbf{r}_b &= [z_b \sin(\theta) \quad -z_b \sin(\phi) \quad z_b]^T \\ \mathbf{r}_w &= [-z_w \sin(\theta) \quad z_w \sin(\phi) \quad z_w]^T \end{aligned} \tag{24}$$

2.3.6. Control Forces and Moments

HAUV prototypes with a single power system typically use aerial propellers, as experimental studies have shown that aerial propellers can achieve underwater propulsion to a certain extent. The two propellers of the coaxial HAUV are fixed to a vector tilt device, and the vector platform controls the output of force and torque by controlling the tilt angle. The control input can be expressed as follows [32,52]:

$$\boldsymbol{\tau}_p = \begin{bmatrix} T_x \\ T_y \\ T_z \end{bmatrix} = \mathbf{R}(\delta_x, \delta_y) \begin{bmatrix} 0 \\ 0 \\ k_\alpha \omega_1^2 + \sigma k_\beta \omega_2^2 \end{bmatrix} \tag{25}$$

$$\mathbf{R}(\delta_x, \delta_y) = \begin{bmatrix} \cos \delta_y & -\sin \delta_y \sin \delta_x & -\sin \delta_y \cos \delta_x \\ 0 & \cos \delta_x & -\sin \delta_x \\ \sin \delta_y & \cos \delta_y \sin \delta_x & \cos \delta_x \cos \delta_y \end{bmatrix} \tag{26}$$

$$\boldsymbol{\tau}_\Theta = \begin{bmatrix} u_2 \\ u_3 \\ u_4 \end{bmatrix} = \begin{bmatrix} -d \sin \delta_x (k_\alpha \omega_1^2 + \sigma k_\beta \omega_2^2) \\ -d \sin \delta_y \cos \delta_x (k_\alpha \omega_1^2 + \sigma k_\beta \omega_2^2) \\ \gamma_\alpha \omega_1^2 + \gamma_\beta \omega_2^2 \end{bmatrix} \tag{27}$$

where k_α and are the lift coefficients of the upper and lower propellers, respectively. σ is the lower propeller lift loss coefficient. d is the length from the lift center to the center of mass. $\mathbf{R}(\delta_x, \delta_y)$ is the mapping transformation matrix of the propeller thrust to the body-fixed coordinate system. δ_x and δ_y indicate the angles of declination of the vector tilting device.

Remark 2. From the point of view of actual flight control, the oscillating turn angle of the vector tilting platform is so small that we can approximate it as $\cos \delta_x \approx 1, \cos \delta_y \approx 1, \sin \delta_x \approx \delta_x \approx 0, \sin \delta_y \approx \delta_y \approx 0$. In this case, the control input can be rewritten to consider only the main factors. The T_x and T_y values are small compared to the T_z value such that the effects of T_x and T_y can be ignored. For convenience, T_z is redefined as u_1 .

$$u_1 = T_z = (k_\alpha \omega_1^2 + \sigma k_\beta \omega_2^2) \cos \delta_x \cos \delta_y \tag{28}$$

Through the above directions, the force generated by the action mechanism can be rewritten in the following vector form:

$$\boldsymbol{\tau}_v = [\boldsymbol{\tau}_p^T \quad \boldsymbol{\tau}_\Theta^T]^T = [0 \quad 0 \quad u_1 \quad u_2 \quad u_3 \quad u_4]^T \tag{29}$$

τ_p and τ_Θ are the actual control inputs of the position and attitude subsystems, respectively. It is obvious that the position subsystem has only one control input to control the 3-degree-of-freedom (DOF) translational motion, which is a typical underactuated system; meanwhile, the attitude subsystem is a fully driven system. For the whole coaxial HAUV system, the translational motion depends on the cooperative change in the attitude angle. The coaxial HAUV system is a typical underdriven, strongly coupled motion system, which leads to great challenges when designing a controller for it.

2.3.7. Analysis of Mathematical Model of Multiple Interference

Coaxial HAUVs are relatively small in size and are highly susceptible to internal and external disturbances, which prevent them from following the intended trajectory while navigating. The compound disturbances of wind, waves, and currents in the external environment play an even more decisive role in affecting coaxial HAUVs with a light mass and a small volume. In this section, the wind, wave, and current disturbances are modeled and discussed, and the proposed disturbance mathematical model is used in a simulation; this makes the simulation experiments closer to the actual situation and thus increases their research value.

1 Sea breeze disturbance

Sea wind can cause a coaxial HAUV to yaw while traveling. Sea wind can both set off waves and generate corresponding forces and moments on the coaxial HAUV body, thus changing the trajectory of the coaxial HAUV. Sea wind interference can be divided into average (constant) wind interference and pulsating wind interference, but only the effect of constant wind is considered in practice. Additional disturbance forces on coaxial HAUVs are caused by constant wind disturbance F_{wind} and M_{wind} can be described as follows:

$$\begin{aligned} F_{wind} &= -C_{dwind} \circ |v_r| \circ v_r \\ M_{wind} &= r_w \times F_{wind} \end{aligned} \quad (30)$$

\circ is the Hadamard product (elemental multiplication) [34]. The constant wind is assumed to have a constant inertial reference velocity $v_w \in R^3$; then, the relative velocity of the coaxial HAUV in the wind is $v_r = v_1 - v_w$. The wind acts on the geometric center of the coaxial HAUV body exposed to the air, that is, the center of wind pressure action, which is represented as $r_w \in R^3$, and C_{dwind} represents the wind damping coefficient.

2. Ocean current interference

From the perspective of time, ocean currents can be divided into steady flow and unsteady flow, and, from the perspective of geography, they can be divided into uniform flow and non-uniform flow. The effect of the current is similar to that of the sea breeze, and its magnitude is proportional to the square of the relative velocity. In general, ocean currents are slowly time-varying, and the force F_c and moment M_c generated by the current can be expressed as follows:

$$\begin{aligned} F_c &= -C_{dc} \circ |v_{rc}| \circ v_{rc} \\ M_c &= r_b \times f_c \end{aligned} \quad (31)$$

Ocean currents are generally considered to be constant and uniform; assuming that they have a constant inertial reference speed $v_c \in R^3$, $v_{rc} = v_1 - v_c$ is the relative velocity of the coaxial HAUV in the current and C_{dc} represents the water damping coefficient.

3. Ocean wave interference

Wave disturbances are complex; generally formed by natural conditions such as wind, tsunamis, and tides; and may change with seasonal variations, water area, wind strength, etc. From the study of near-surface waves, it can be seen that irregular waves can be regarded as the superposition of a large number of uniformly small waves, and, among these small waves, the ones that have the main influence on the motion of the HAUV are the long peaked random waves with a period between 5–20 s. In order to simplify the

problem, wave interference caused by a single-frequency micro-amplitude long peak wave with a fixed direction (propagating along the X- and Y-axes of the inertial system) can be considered the main concern. In this context, linear wave theory (i.e., Airy Theory) may be preferred. Wave interference caused by single-frequency micro-amplitude long peak waves with a fixed direction is considered. It is assumed that these waves are regular waves concentrated in the x_e -axis and y_e -axis directions [34].

The wave corresponding velocity potential functions Γ_x and Γ_y are expressed as follows

$$\begin{aligned} \Gamma_x &= \sum_{i=1}^N \frac{gA_{xi}}{\omega_{xi}} e^{k_{xi}z} \sin(k_{xi}x - \omega_{xi}t + \varphi_{xi}) \\ \Gamma_y &= \sum_{i=1}^N \frac{gA_{yi}}{\omega_{yi}} e^{k_{yi}z} \sin(k_{yi}y - \omega_{yi}t + \varphi_{yi}) \end{aligned} \tag{32}$$

where N , A_{ji} , ω_{ji} , k_{ji} , and $\varphi_{ji}(j = x, y)$ are the total number of waves, wave amplitude, wave frequency, wave number, and phase. A simple dispersion relation is satisfied between the wave number and the circular frequency of a wave, i.e., $k_{ji} = \omega_{ji}^2/g$ [31].

The transverse and vertical velocities of the wave in the x_e -axis and y_e -axis directions and the corresponding accelerations are given by the following equation:

$$\begin{aligned} u_x &= \frac{\partial \Gamma_x}{\partial x}, w_x = \frac{\partial \Gamma_x}{\partial z}, u_y = \frac{\partial \Gamma_y}{\partial y}, w_y = \frac{\partial \Gamma_y}{\partial z} \\ \dot{u}_x &= \frac{\partial u_x}{\partial t}, \dot{w}_x = \frac{\partial w_x}{\partial t}, \dot{u}_y = \frac{\partial u_y}{\partial t}, \dot{w}_y = \frac{\partial w_y}{\partial t} \end{aligned} \tag{33}$$

The scale of the proposed coaxial HAUV is very small compared with that of the long peak waves in the ocean, so the effect of the vehicle on the incident wave pressure field can be neglected. In addition, a significant feature of coaxial HAUVs is that the submerged part of the body changes in the process of cross-domain maneuvering, which leads to the wave action of the body also changing. Therefore, the wave loads encountered by the coaxial HAUV can be calculated according to the following equation [37]:

$$\begin{aligned} F_{wave,x} &= \int_{L_z} (\rho_w C_m \pi R^2 \dot{u}_x + \frac{1}{2} \rho_w C_d R u_x |u_x|) dz \\ F_{wave,y} &= \int_{L_z} (\rho_w C_m \pi R^2 \dot{u}_y + \frac{1}{2} \rho_w C_d R u_y |u_y|) dz \end{aligned} \tag{34}$$

$$\begin{aligned} \mathbf{M}_{wave} &= \mathbf{r}_b \times \mathbf{F}_{wave} \\ \mathbf{F}_{wave} &= \mathbf{J}_1^T [F_{wave,x} \quad F_{wave,y} \quad 0]^T \end{aligned} \tag{35}$$

where L_z is the length of being submerged.

Remark 3. As the external environment affects the motion of the coaxial HAUV, mathematical models of wind, waves, and currents are developed, and they are added to the simulation experiments for motion control. Based on a detailed analysis of the various external forces and moments applied to the system in the previous subsection, they can be classified as follows: The first category consists of the active control forces that need to be regulated by the controller, i.e., the control forces and control moments $\boldsymbol{\tau}_v$; the second category consists of external forces that can be measured or approximated, such as Coriolis forces \mathbf{C}_v , restoring forces \mathbf{g}_v , and damping forces \mathbf{D}_v ; and the third category consists of terms that are not practically measurable or are extremely expensive to model accurately, such as the wind disturbance forces \mathbf{F}_{wind} and \mathbf{M}_{wind} , the wave disturbance forces \mathbf{F}_{wave} and \mathbf{M}_{wave} , and the current-generated forces \mathbf{F}_c and \mathbf{M}_c . The third type of external forces can be approximated using empirical formulas, but it is very difficult to obtain real-time information about the marine environment with limited accuracy [33].

2.4. Modeling of Coaxial HAUV Cross-Domain Maneuvering Dynamics

HAUVs, as newly emerging marine amphibious robots, are subjected to external forces similar to underwater robots and drones, depending on the environmental medium and navigation state. They are affected by the three generalized forces and corresponding torques analyzed above. The coaxial HAUV can be modeled as a hybrid system (consisting

of an underwater model, an air model, and a transition-state model) in which the dynamics of the HAUV change depending on the ambient medium (air or water).

Referring to relevant experience with underwater robots, translating the above model (12) into an inertial coordinate system gives the following [50]:

$$\begin{cases} \dot{\eta} = \dot{\eta} \\ M_{\eta} \ddot{\eta} + C_{\eta} \dot{\eta} + D_{\eta} \dot{\eta} + g_{\eta} = \tau_{\eta} + \tau_{d\eta} \end{cases} \quad (36)$$

The transformed variables satisfy the following relationship: $M_{\eta} = J^{-T} M J^{-1}$, $C_{\eta} = J^{-T} (C - M J^{-1} \dot{J}) J^{-1}$, $D_{\eta} = J^{-T} D J^{-1}$, $g_{\eta} = J^{-T} g_v$, $\tau_{d\eta} = J^{-T} \tau_{d_v}$, $\tau_{\eta} = J^{-T} \tau_v$.

Further simplification and rewriting of (36) gives the form of the following second-order state space equation:

$$\begin{cases} \dot{\eta} = \dot{\eta} \\ \ddot{\eta} = f + u + d \end{cases} \quad (37)$$

where $f = -M_{\eta}^{-1} (C_{\eta} \dot{\eta} + D_{\eta} \dot{\eta} + g_{\eta})$ represents the hydrodynamically relevant nonlinear function transferred to the inertial coordinate system, containing the mass matrix, Coriolis force term, damping term, and restoring force term; $u = M_{\eta}^{-1} \tau_{\eta} = M_{\eta}^{-1} J^{-T} \tau_v$ indicates the control inputs transferred to the inertial system; and $d = M_{\eta}^{-1} \tau_{d\eta}$, $d = [d_x \ d_y \ d_z \ d_{\phi} \ d_{\theta} \ d_{\psi}]^T$ represents the aggregate uncertainty of the system, including the model parameter jumping change, variate linearization approximation errors, and difficult-to-calculate fluid disturbance forces and moments.

Assumption 2 [53]. *With reference to near-surface motion marine robots, the ensemble uncertainty arising from the marine environment and model lumped uncertainty $d = [d_p^T \ d_{\Theta}^T]^T$ and its derivatives are bounded; that is, there exists an unknown positive constant D , satisfying $\|d\| \leq D$. Further analysis can consider that the elements of d under each DOF $d_i, i = x, y, \dots, \psi$ satisfy $|d_i| \leq D_i$ and that D_i is the uncertainty upper bound of the corresponding DOF.*

Remark 4. *Referring to the control logic of coaxial UAVs, the coaxial HAUV is a 6-DOF motion system with four control inputs $\tau_v = [\tau_p^T \ \tau_{\Theta}^T]^T$. $\tau_p = [0 \ 0 \ u_1]^T$ and $\tau_{\Theta} = [u_2 \ u_3 \ u_4]^T$ are the control inputs for the position and attitude subsystems, respectively. After transforming the dynamical equations into the inertial coordinate system, the control inputs of the position subsystem in the inertial system are $u_p = M_{\eta 1}^{-1} J_1^{-T} \tau_p$, where $M_{\eta 1} = J_1^{-T} M_{11} J_1^{-1}$.*

The HAUV system is decomposed into a cascade of inner and outer ring systems and $u_p = [u_x \ u_y \ u_z]^T$ is defined as a virtual control law. The variation in the attitude angle of the coaxial HAUV causes the total lift to produce a horizontal component in the inertial coordinate system, which allows the coaxial HAUV to produce a horizontal maneuver. By giving the desired yaw angle ψ_d and after acquiring the virtual control law u_p , the total lift u_1 and the desired pitch angle θ_d and roll angle ϕ_d can be obtained by inversely solving the following [54]:

$$\begin{cases} u_1 = \tau_p(3), \tau_p = J_1^T M_{\eta 1} u_p \\ \theta_d = \arctan\left(\frac{u_x \cos \psi_d + u_y \sin \psi_d}{u_z}\right) \\ \phi_d = \arctan\left(\frac{(u_x \sin \psi_d - u_y \cos \psi_d) \cos \theta_d}{u_z}\right) \end{cases} \quad (38)$$

3. Design of Fixed-Time Composite Robust Controller

In this section, we present the design of an RBFNN-based adaptive fixed-time sliding mode controller (NNAFTSMC) for the coaxial HAUV. Firstly, a fixed-time terminal sliding mode control (FTSMC) scheme is proposed to design the basic controller. It should be emphasized that, although the dynamics of the HAUV were analyzed during the modeling

phase, it is extremely difficult to obtain effective model parameters in real time to construct the dynamic characteristics of HAUVs. Next, six RBFNN approximators are used to identify the 6-DOF nonlinear dynamic functions online. On this basis, the adaptive algorithm is used to estimate the weight parameters of the RNFNN and the controller’s robust switching terms.

3.1. RBFNN Approximation Algorithm

Because of the excellent performance of the RBFNN in nonlinear function approximation, it is widely used in nonlinear function estimation in the control field. The RBFNN has an outstanding local approximation ability, can effectively avoid local minima, and has faster learning convergence. In this paper, except for the mass matrix in Equation (14), which is known due to it being relatively easy to obtain, the remaining hydrodynamic parameters are unknown by default and are identified online using the RBFNN. At the same time, its network structure is shown in Figure 5.

Any continuous function can be accurately identified using the RBFNN, and the lumped uncertainty of the coaxial HAUV can be approximated using the RBFNN technique. The RBFNN can well approximate the nonlinear function of Equation (32), which is composed of time-varying hydrodynamic parameters and external perturbations, that is, $F = f + d$; the relationship shown in the following equation is satisfied:

$$F = W^T h + \varepsilon \tag{39}$$

Assumption 3. From the conclusion of assumption 2, the total uncertainty of the set generated by the marine environment and model hydrodynamics is bounded. Further, by using the RBFNN to approximate the nonlinear function F , theoretically, the approximation error ε can be arbitrarily small. ε satisfies $\|\varepsilon\| \leq \varepsilon_{max}$, $|\varepsilon_i| \leq \varepsilon_{imax}$, $i = 1, 2, \dots, 6$, and ε_{imax} is the maximum reconstruction error at each DOF.

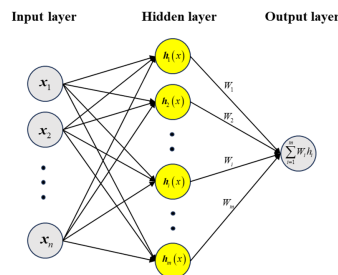


Figure 5. RBFNN structure diagram.

3.2. RBFNN-Based Adaptive Fixed-Time Sliding Mode Controller Design

3.2.1. Fixed-Time Sliding Mode Controller Designing

In this section, a basic fixed-time sliding mode controller is proposed to ensure that the system converges to the desired position at a fixed time. The controller should output effective control signals to track the reference trajectory under complex working conditions. When designing the reference trajectory, it is necessary to make the trajectory as smooth, bounded, and derivable as possible. The desired position and attitude are expressed as $\eta_d = [\eta_{1d}^T \ \eta_{2d}^T]^T$, $\eta_{1d} = [x_d \ y_d \ z_d]^T$, $\eta_{2d} = [\phi_d \ \theta_d \ \psi_d]^T$. For the convenience of describing the error control process, the control error is defined as $e = \eta - \eta_d$.

Control objective: The goal is to design the control input τ_v such that

$$\lim_{t \rightarrow +\infty} \begin{pmatrix} e \\ \dot{e} \end{pmatrix} = \mathbf{0}^{12 \times 1} \tag{40}$$

The fixed-time fast terminal sliding surface is selected for the position and attitude loop as follows:

$$s = \dot{e} + k_1 e + k_2 \tanh(e) + k_3 \text{sig}^\gamma(e) \tag{41}$$

where k_1, k_2 , and k_3 are the matrices of the parameters of the sliding mode surface to be designed, respectively. k_1, k_2 , and k_3 are six-dimensional positive definite diagonal matrices, and $\gamma > 1$.

Through a simple mathematical calculation, the time derivative of the sliding mode surface s is calculated as follows:

$$\begin{aligned} \dot{s} &= \ddot{e} + k_1 \dot{e} + k_2 \left(1 - \tanh(e)^T \tanh(e)\right) \dot{e} + k_3 \gamma \text{sig}^{\gamma-1}(e) \dot{e} \\ &= (f + u + d - \ddot{\eta}_d) + H(e, \dot{e}) \end{aligned} \tag{42}$$

where $H(e, \dot{e}) = \left(k_1 + k_2 \left(1 - \tanh(e)^T \tanh(e)\right) + k_3 \gamma \text{sig}^{\gamma-1}(e)\right) \dot{e}$.

By letting $\dot{s} = 0$, the equivalent control law can be obtained, combining the isokinetic reaching law and the exponential convergence law to obtain a controller for the attitude and position loop, respectively, as follows:

$$u = \ddot{\eta}_d - \hat{F} - H(e, \dot{e}) - \hat{\varepsilon} \text{sign}(s) - c_1 \text{sig}^{\frac{p}{q}}(s) - c_2 \text{sig}^{\frac{m}{n}}(s) - c_3 s \tag{43}$$

where $\hat{F} = \hat{W}^T h$ is the estimated value of F ; $\hat{\varepsilon}$ is an estimate of the upper bound of the reconstruction error; $c_1 > 0, c_2 > 0$, and $c_3 > 0$ are the parameters to be designed for the reaching law; and p, q, m , and n are positive odd numbers and satisfy $0 < p < q, m > n > 0$.

Remark 5. It is worth noting that the solved controller is not the real control input. Consider that the control inputs in the inertial system satisfy the relationship $u = M_\eta^{-1} \tau_\eta = M_\eta^{-1} J^{-T} \tau_v$; then, the actual control input should be solved as follows:

$$\tau_v = J^T M_\eta u \tag{44}$$

3.2.2. Adaptive Law Design

The robustness of the control system can be further improved by selecting the appropriate robust switching gain; therefore, the adaptive law is designed to compensate for the remaining neural network approximation error ε . The ideal weight coefficients of neural networks W are difficult to obtain intuitively; therefore, the weight coefficient needs to be obtained by using adaptive technology. \hat{W} and $\hat{\varepsilon}$ are the estimated values of W and ε , $\tilde{W} = W - \hat{W}$ and $\tilde{\varepsilon} = \varepsilon - \hat{\varepsilon}$ are defined as the respective estimation errors. The adaptive law under each DOF is designed as follows [55]:

$$\begin{aligned} \dot{\hat{W}} &= \begin{bmatrix} \dot{\hat{W}}_1 & \dot{\hat{W}}_2 & \dots & \dot{\hat{W}}_6 \end{bmatrix} \\ \dot{\hat{W}}_i &= \gamma_1 (s_i h_i - \mu_1 \hat{W}_i), i = 1, 2, \dots, 6 \end{aligned} \tag{45}$$

$$\begin{aligned} \dot{\hat{\varepsilon}} &= \begin{bmatrix} \dot{\hat{\varepsilon}}_1 & \dot{\hat{\varepsilon}}_2 & \dots & \dot{\hat{\varepsilon}}_6 \end{bmatrix}^T \\ \dot{\hat{\varepsilon}}_i &= \gamma_2 (|s_i| - \mu_2 \hat{\varepsilon}_i), i = 1, 2, \dots, 6 \end{aligned} \tag{46}$$

where $\gamma_1, \gamma_2, \mu_1$, and μ_2 are the designed positive definite coefficient matrices. Subscript $i = 1, 2, \dots, 6$ indicates six DOFs, such as x, y, \dots, ψ .

3.3. Stability Proofs and Analyses

Theorem 1. Consider the coaxial HAUV system. If NN fixed-time controller (43) and adaptive laws (45) and (46) are adopted, then the sliding mode surface will asymptotically reach a neighborhood of 0. $s, \tilde{W}_i, \tilde{\varepsilon}_i$ is consistently terminal-bounded in this case.

Proof of Theorem 1. The Lyapunov function is designed as follows:

$$V_1 = \frac{1}{2} \mathbf{s}^T \mathbf{s} + \frac{1}{2} \text{tr} \{ \tilde{\mathbf{W}}^T \gamma_1^{-1} \tilde{\mathbf{W}} \} + \frac{1}{2\gamma_2} \tilde{\boldsymbol{\varepsilon}}^T \tilde{\boldsymbol{\varepsilon}} \tag{47}$$

By solving the time derivative of Equation (47),

$$\begin{aligned} \dot{V}_1 &= \mathbf{s}^T \dot{\mathbf{s}} - \frac{1}{\gamma_1} \sum_{i=1}^6 \tilde{\mathbf{W}}_i^T \dot{\tilde{\mathbf{W}}}_i - \frac{1}{\gamma_2} \sum_{i=1}^6 \tilde{\boldsymbol{\varepsilon}}_i \dot{\tilde{\boldsymbol{\varepsilon}}}_i \\ &= \mathbf{s}^T \left(\dot{\mathbf{e}} + k_1 \dot{\mathbf{e}} + k_2 (1 - \tanh(\mathbf{e}))^T \tanh(\mathbf{e}) \dot{\mathbf{e}} + k_3 \gamma \text{sig}^{\gamma-1}(\mathbf{e}) \dot{\mathbf{e}} \right) \\ &\quad - \frac{1}{\gamma_1} \sum_{i=1}^6 \tilde{\mathbf{W}}_i^T \dot{\tilde{\mathbf{W}}}_i - \frac{1}{\gamma_2} \sum_{i=1}^6 \tilde{\boldsymbol{\varepsilon}}_i \dot{\tilde{\boldsymbol{\varepsilon}}}_i \\ &= \mathbf{s}^T (\mathbf{f} + \mathbf{u} + \mathbf{d} - \ddot{\boldsymbol{\eta}}_d + \mathbf{H}(\mathbf{e}, \dot{\mathbf{e}})) - \frac{1}{\gamma_1} \sum_{i=1}^6 \tilde{\mathbf{W}}_i^T \dot{\tilde{\mathbf{W}}}_i - \frac{1}{\gamma_2} \sum_{i=1}^6 \tilde{\boldsymbol{\varepsilon}}_i \dot{\tilde{\boldsymbol{\varepsilon}}}_i \\ &= \mathbf{s}^T (\mathbf{F} + \mathbf{u} - \ddot{\boldsymbol{\eta}}_d + \mathbf{H}(\mathbf{e}, \dot{\mathbf{e}})) - \frac{1}{\gamma_1} \sum_{i=1}^6 \tilde{\mathbf{W}}_i^T \dot{\tilde{\mathbf{W}}}_i - \frac{1}{\gamma_2} \sum_{i=1}^6 \tilde{\boldsymbol{\varepsilon}}_i \dot{\tilde{\boldsymbol{\varepsilon}}}_i \\ &= \mathbf{s}^T (\mathbf{u} + \mathbf{W}^T \mathbf{h} + \boldsymbol{\varepsilon} - \ddot{\boldsymbol{\eta}}_d + \mathbf{H}(\mathbf{e}, \dot{\mathbf{e}})) - \frac{1}{\gamma_1} \sum_{i=1}^6 \tilde{\mathbf{W}}_i^T \dot{\tilde{\mathbf{W}}}_i - \frac{1}{\gamma_2} \sum_{i=1}^6 \tilde{\boldsymbol{\varepsilon}}_i \dot{\tilde{\boldsymbol{\varepsilon}}}_i \end{aligned} \tag{48}$$

By substituting controller (43) \mathbf{u} into \dot{V}_1 , the following can be obtained:

$$\begin{aligned} \dot{V}_1 &= \mathbf{s}^T \left(\ddot{\boldsymbol{\eta}}_d - \hat{\mathbf{W}}^T \mathbf{h} - \mathbf{H}(\mathbf{e}, \dot{\mathbf{e}}) + \mathbf{W}^T \mathbf{h} + \boldsymbol{\varepsilon} - \ddot{\boldsymbol{\eta}}_d + \mathbf{H}(\mathbf{e}, \dot{\mathbf{e}}) \right. \\ &\quad \left. - \hat{\boldsymbol{\varepsilon}} \text{sign}(\mathbf{s}) - c_1 \text{sig}^q(\mathbf{s}) - c_2 \text{sig}^{\frac{m}{n}}(\mathbf{s}) - c_3 \mathbf{s} \right) - \frac{1}{\gamma_1} \sum_{i=1}^6 \tilde{\mathbf{W}}_i^T \dot{\tilde{\mathbf{W}}}_i - \frac{1}{\gamma_2} \sum_{i=1}^6 \tilde{\boldsymbol{\varepsilon}}_i \dot{\tilde{\boldsymbol{\varepsilon}}}_i \\ &= \mathbf{s}^T \left(\tilde{\mathbf{W}}^T \mathbf{h} + \boldsymbol{\varepsilon} - \hat{\boldsymbol{\varepsilon}} \text{sign}(\mathbf{s}) - c_1 \text{sig}^q(\mathbf{s}) - c_2 \text{sig}^{\frac{m}{n}}(\mathbf{s}) - c_3 \mathbf{s} \right) \\ &\quad - \frac{1}{\gamma_1} \sum_{i=1}^6 \tilde{\mathbf{W}}_i^T \dot{\tilde{\mathbf{W}}}_i - \frac{1}{\gamma_2} \sum_{i=1}^6 \tilde{\boldsymbol{\varepsilon}}_i \dot{\tilde{\boldsymbol{\varepsilon}}}_i \end{aligned} \tag{49}$$

By substituting the adaptive laws (45) and (46) into the above equation, we obtain the following:

$$\begin{aligned} \dot{V}_1 &= \mathbf{s}^T \left(\tilde{\mathbf{W}}^T \mathbf{h} + \boldsymbol{\varepsilon} - \hat{\boldsymbol{\varepsilon}} \text{sign}(\mathbf{s}) - c_1 \text{sig}^q(\mathbf{s}) - c_2 \text{sig}^{\frac{m}{n}}(\mathbf{s}) - c_3 \mathbf{s} \right) \\ &\quad - \frac{1}{\gamma_1} \sum_{i=1}^6 \tilde{\mathbf{W}}_i^T \dot{\tilde{\mathbf{W}}}_i - \frac{1}{\gamma_2} \sum_{i=1}^6 \tilde{\boldsymbol{\varepsilon}}_i \dot{\tilde{\boldsymbol{\varepsilon}}}_i \\ &\leq \sum_{i=1}^6 s_i \tilde{\mathbf{W}}_i^T \mathbf{h}_i + \sum_{i=1}^6 |s_i| |\tilde{\boldsymbol{\varepsilon}}_i| - c_1 \|\mathbf{s}\|^{\frac{p+q}{q}} - c_2 \|\mathbf{s}\|^{\frac{m+n}{n}} - c_3 \|\mathbf{s}\|^2 \\ &\quad - \frac{1}{\gamma_1} \sum_{i=1}^6 \tilde{\mathbf{W}}_i^T (\gamma_1 s_i \mathbf{h}_i - \gamma_1 \mu_1 \tilde{\mathbf{W}}_i) - \frac{1}{\gamma_2} \sum_{i=1}^6 \tilde{\boldsymbol{\varepsilon}}_i (\gamma_2 |s_i| - \gamma_2 \mu_2 \tilde{\boldsymbol{\varepsilon}}_i) \\ &\leq -c_1 \|\mathbf{s}\|^{\frac{p+q}{q}} - c_2 \|\mathbf{s}\|^{\frac{m+n}{n}} - c_3 \|\mathbf{s}\|^2 + \mu_1 \sum_{i=1}^6 \tilde{\mathbf{W}}_i^T \tilde{\mathbf{W}}_i + \mu_2 \sum_{i=1}^6 \tilde{\boldsymbol{\varepsilon}}_i \tilde{\boldsymbol{\varepsilon}}_i \end{aligned} \tag{50}$$

Here, the results and properties of the term $\mu_1 \sum_{i=1}^6 \tilde{W}_i^T \hat{W}_i + \mu_2 \sum_{i=1}^6 \tilde{\varepsilon}_i \hat{\varepsilon}_i$ are discussed. According to the relevant conclusion of Young's inequality $\tilde{W}_i^T \hat{W}_i, \tilde{\varepsilon}_i \hat{\varepsilon}_i$ terms satisfy the following inequality:

$$\begin{aligned} \tilde{W}_i^T \hat{W}_i &= \tilde{W}_i^T (\mathbf{W}_i - \tilde{W}_i) \\ &\leq \left(\tilde{W}_i^T \tilde{W}_i / 2 + \mathbf{W}_i^T \mathbf{W}_i / 2 - \tilde{W}_i^T \tilde{W}_i \right) \\ &\leq -\tilde{W}_i^T \tilde{W}_i / 2 + \mathbf{W}_i^T \mathbf{W}_i / 2 \\ \tilde{\varepsilon}_i \hat{\varepsilon}_i &\leq -\tilde{\varepsilon}_i^2 / 2 + \varepsilon_i^2 / 2 \end{aligned} \tag{51}$$

According to the conclusion obtained from the above analysis, Equation (50) can be further simplified and rewritten as follows:

$$\begin{aligned} \dot{V}_1 &\leq -c_1 \|s\|^{\frac{p+q}{q}} - c_2 \|s\|^{\frac{m+n}{n}} - c_3 \|s\|^2 - \frac{\mu_1}{2} \sum_{i=1}^6 \tilde{W}_i^T \tilde{W}_i - \frac{\mu_2}{2} \sum_{i=1}^6 \tilde{\varepsilon}_i^2 \\ &\quad + \frac{\mu_1}{2} \sum_{i=1}^6 \mathbf{W}_i^T \mathbf{W}_i + \frac{\mu_2}{2} \sum_{i=1}^6 \varepsilon_i^2 \\ &\leq -c_3 \|s\|^2 - \frac{\mu_1}{2} \sum_{i=1}^6 \tilde{W}_i^T \tilde{W}_i - \frac{\mu_2}{2} \sum_{i=1}^6 \tilde{\varepsilon}_i^2 + \Delta_1 \\ &\leq -2c_3 \left(\frac{1}{2} s^T s \right) - \mu_1 \gamma_1 \left(\frac{1}{2\gamma_1} \sum_{i=1}^6 \tilde{W}_i^T \tilde{W}_i \right) - \mu_2 \gamma_2 \left(\frac{1}{2\gamma_2} \sum_{i=1}^6 \tilde{\varepsilon}_i^2 \right) + \Delta_1 \\ &\leq -\rho_1 V_1 + \Delta_1 \end{aligned} \tag{52}$$

where $\Delta_1 = \frac{\mu_1}{2} \sum_{i=1}^6 \mathbf{W}_i^T \mathbf{W}_i + \frac{\mu_2}{2} \sum_{i=1}^6 \varepsilon_i^2, \rho_1 = \min\{2c_3, \mu_1 \gamma_1, \mu_2 \gamma_2\}$. On the basis of Lyapunov theorem and Lemma 1, $s, \tilde{W}_i, \tilde{\varepsilon}_i$ is consistently terminal-bounded. Further, considering that s is defined in terms of vectors, it can be concluded that the control error is also bounded. It can be concluded that the designed controller can guarantee that the global system is bounded and asymptotically convergent, but it cannot guarantee the achievement of fixed-time convergence.

Next, the actual fixed-time stability of the global system is proven.

As the domain of the Gaussian function belongs to the interval $[0, 1]$, the activation function h is also bounded.

According to the above analysis, $\tilde{W}^T h$ is bounded and satisfies the following relationship:

$$\left\| \tilde{W}^T h \right\| \leq \left\| \tilde{W} \right\| \|h\| \tag{53}$$

As an adaptive strategy is adopted to approximate the upper bound of the neural network error ε to ensure the robustness of the controller, the adaptive parameter $\hat{\varepsilon}$ will continue to increase until it completely cancels out the approximation error; then, it can be assumed that there exists an adaptive parameter $\hat{\varepsilon}$ such that the following relationship holds:

$$\left\| \tilde{W}^T h + \varepsilon \right\| \leq \|\hat{\varepsilon}\| \tag{54}$$

□

Theorem 2. Considering system (37), Equation (41) is chosen as the terminal sliding mode surface, Equation (43) is the controller, and (45) and (46) are the adaptive update laws. Then, the sliding mode surface reaches a region close to 0 at a fixed time T_1 . Once the sliding mode surface satisfies $s = 0$, the actual control error also converges to 0 at a practically fixed time T_2 .

Proof of Theorem 2. The proof process is divided into two steps: the first step is to show that the arrival phase can reach 0 at a fixed time T_1 , and the second step is to show that the tracking error in the sliding phase reaches 0 at a practically fixed time T_2 . The Lyapunov function is constructed as follows:

$$V_2 = \frac{1}{2} \mathbf{s}^T \mathbf{s} \tag{55}$$

By taking the derivative of Equation (55) and substituting controller (43) \mathbf{u} into (56), one obtains

$$\begin{aligned} \dot{V}_2 &= \mathbf{s}^T \dot{\mathbf{s}} \\ &= \mathbf{s}^T \left(\ddot{\mathbf{e}} + k_1 \dot{\mathbf{e}} + k_2 \left(1 - \tanh(\mathbf{e})^T \tanh(\mathbf{e}) \right) \dot{\mathbf{e}} + k_3 \gamma \text{sig}^{\gamma-1}(\mathbf{e}) \dot{\mathbf{e}} \right) \\ &= \mathbf{s}^T \left(\mathbf{f} + \mathbf{u} + \mathbf{d} - \ddot{\mathbf{y}}_d + \mathbf{H}(\mathbf{e}, \dot{\mathbf{e}}) \right) \\ &= \mathbf{s}^T \left(\mathbf{f} + \mathbf{d} - \ddot{\mathbf{y}}_d + \mathbf{H}(\mathbf{e}, \dot{\mathbf{e}}) + \ddot{\mathbf{y}}_d - \hat{\mathbf{F}} - \mathbf{H}(\mathbf{e}, \dot{\mathbf{e}}) - \hat{\boldsymbol{\varepsilon}} \text{sign}(\mathbf{s}) \right. \\ &\quad \left. - c_1 \text{sig}^{\frac{p}{q}}(\mathbf{s}) - c_2 \text{sig}^{\frac{m}{n}}(\mathbf{s}) - c_3 \mathbf{s} \right) \\ &= \mathbf{s}^T \left(\tilde{\mathbf{F}} + \boldsymbol{\varepsilon} - \hat{\boldsymbol{\varepsilon}} \text{sign}(\mathbf{s}) - c_1 \text{sig}^{\frac{p}{q}}(\mathbf{s}) - c_2 \text{sig}^{\frac{m}{n}}(\mathbf{s}) - c_3 \mathbf{s} \right) \\ &= \mathbf{s}^T \left(\left(\tilde{\mathbf{W}}^T \mathbf{h} + \boldsymbol{\varepsilon} \right) - \hat{\boldsymbol{\varepsilon}} \text{sign}(\mathbf{s}) - c_1 \text{sig}^{\frac{p}{q}}(\mathbf{s}) - c_2 \text{sig}^{\frac{m}{n}}(\mathbf{s}) - c_3 \mathbf{s} \right) \\ &\leq \|\mathbf{s}\| \left\| \tilde{\mathbf{W}}^T \mathbf{h} + \boldsymbol{\varepsilon} \right\| - \|\mathbf{s}\| \|\hat{\boldsymbol{\varepsilon}}\| - c_1 \|\mathbf{s}\|^{\frac{p+q}{q}} - c_2 \|\mathbf{s}\|^{\frac{m+n}{n}} - c_3 \|\mathbf{s}\| \end{aligned} \tag{56}$$

By taking into account the properties of the adaptive gain, we obtain the following:

$$\begin{aligned} \dot{V}_2 &\leq -c_1 \|\mathbf{s}\|^{\frac{p+q}{q}} - c_2 \|\mathbf{s}\|^{\frac{m+n}{n}} - c_3 \|\mathbf{s}\| \\ &\leq -c_1 \|\mathbf{s}\|^{\frac{p+q}{q}} - c_2 \|\mathbf{s}\|^{\frac{m+n}{n}} \\ &\leq -2^{\frac{p+q}{2q}} c_1 \left(\frac{1}{2} \mathbf{s}^T \mathbf{s} \right)^{\frac{p+q}{2q}} - 2^{\frac{m+n}{2n}} c_2 \left(\frac{1}{2} \mathbf{s}^T \mathbf{s} \right)^{\frac{m+n}{2n}} \\ &\leq -\rho_{21} V_2^{\frac{p+q}{2q}} - \rho_{22} V_2^{\frac{m+n}{2n}} \end{aligned} \tag{57}$$

where $\rho_{21} = 2^{\frac{p+q}{2q}} c_1$, $\rho_{22} = 2^{\frac{m+n}{2n}} c_2$.

According to Lemma 3, it can be assumed that, in the reaching phase, the sliding mode surface \mathbf{s} can converge to the neighborhood of 0 at a fixed time T_1 , $T_1 = \frac{1}{\rho_{21}(1-(p+q)/(2q))} + \frac{1}{\rho_{22}((m+n)/(2n)-1)}$.

Once $\mathbf{s} = 0$ is reached, we can obtain the following:

$$\dot{\mathbf{e}} = -k_1 \mathbf{e} - k_2 \tanh(\mathbf{e}) - k_3 \text{sig}^{\gamma}(\mathbf{e}) \tag{58}$$

In order to prove the sliding phase fixed-time stability of the coaxial HAUV system, a Lyapunov function is chosen as follows:

$$V_3 = \frac{1}{2} \mathbf{e}^T \mathbf{e} \tag{59}$$

Solving the derivatives of V_3 yields the following:

$$\begin{aligned}
 \dot{V}_3 &= e^T \dot{e} \\
 &= e^T (-k_1 e - k_2 \tanh(e) - k_3 \text{sig}^\gamma(e)) \\
 &= -k_1 \|e\|^2 - k_2 e^T \tanh(e) - k_3 \|e\|^{\frac{\gamma+1}{2}} \\
 &\leq -k_1 \|e\|^2 - k_2 \|e\| + 6k_2 \kappa - k_3 \left(\|e\|^2\right)^{\frac{\gamma+1}{2}} \\
 &\leq -k_2 V_3^{\frac{1}{2}} - k_3 V_3^{\frac{\gamma+1}{2}} + \Delta_3
 \end{aligned} \tag{60}$$

where $\Delta_3 = 6k_2 \kappa$, $\kappa = 0.2785$.

According to Lemma 2, in the sliding phase, e can converge to the 0 neighborhood in a practically fixed time T_2 , $T_2 = \frac{1}{k_2(1-1/2)} + \frac{1}{k_3((\gamma+1)/2-1)}$.

In summary, the fixed-time stability of the coaxial HAUV global system is proven, and the system state can converge at a fixed time of $T = T_1 + T_2$ to 0. Above, the stability-proof process of the designed controller in a fixed time is completed.

□

4. Simulation and Discussion

In the previous section, the effectiveness of the NNAFTSMC algorithm for coaxial HAUV cross-domain control was proven in a theoretical analysis. Therefore, the main work presented in this section aimed to verify the stability and effectiveness of the aforementioned controller based on control algorithm simulations. Two different cross-media motion test items were included in the simulation. The first test project aimed to control the coaxial HAUV to achieve a complete water–air amphibious movement; the second experiment project aimed to test the cross-domain tracking effect of different control algorithms controlling the coaxial HAUV.

The most typical cross-domain action was selected—climbing out of water—to test the effect of the proposed control strategy under the conditions of marine environment disturbance and parameter perturbation. The parameters of the coaxial HAUV model used in our simulations are shown in Table A1 in Appendix A. In addition, specific simulation experimental parameters were selected: the fourth-order Runge–Kutta solution method was adopted, and a fixed step size was selected in the solution process, which was set to 0.005.

Meanwhile, the design parameters of the position and attitude loop controllers, adaptive law, and RBFNN were as follows:

Controller design parameters: $k_{1p} = 1.5$, $k_{1\theta} = 2.5$, $k_{2p} = k_{2\theta} = 1.5$, $k_{3p} = k_{3\theta} = 1.0$, $\gamma_p = \gamma_\theta = 5/3$, $c_{1p} = c_{1\theta} = 0.5$, $c_{2p} = c_{2\theta} = 0.5$, $c_{3p} = 1.5$, $c_{3\theta} = 4.5$.

The adaptive law design parameters for the RBFNN were $\mu_{1p} = 0.02$, $\mu_{1\theta} = 0.05$, $\gamma_{1p} = [8, 8, 24]^T$, $\gamma_{1\theta} = [100, 100, 100]^T$. The number of nodes in the hidden layer of the RBFNN was set to $j = 13$, and the center node vector of the Gaussian basis function was denoted as $c = [c_1, c_2, \dots, c_j]$. The c values were taken as shown in Equation (61), and their gains were $\gamma_p = 3.05$ and $\gamma_\theta = 1.55$. The widths of the neurons were $b_p = 6$ and $b_\theta = 5$.

$$c = \gamma \times \begin{bmatrix} -3.0, -2.5, -2.0, -1.5, -1.0, -0.5, 0, 0.5, 1.0, 1.5, 2, 2.5, 3.0 \\ -3.0, -2.5, -2.0, -1.5, -1.0, -0.5, 0, 0.5, 1.0, 1.5, 2, 2.5, 3.0 \\ -3.0, -2.5, -2.0, -1.5, -1.0, -0.5, 0, 0.5, 1.0, 1.5, 2, 2.5, 3.0 \end{bmatrix} \tag{61}$$

The adaptive law design parameters for the robust switching term are $\gamma_{2p} = [2.5, 2.5, 2.5]^T$, $\gamma_{2\theta} = [1.5, 1.5, 1.5]^T$, $\mu_{1p} = 0.05$, $\mu_{1\theta} = 0.02$. In this study, subscripts $(\cdot)_p$ and $(\cdot)_\theta$ are parameters in the position and attitude loops, respectively.

Due to the large difference in the external disturbance force (moment) during coaxial HAUV maneuvering in water–air media, it is difficult to accurately identify the marine

environment and apply it to modeling in practice. The multiple disturbances caused by wind, waves, and currents are analyzed. The effectiveness of controller design can be improved by applying the empirical formula of marine environment simulations given by scholars to simulation research. It is assumed that the disturbances $\tau_{dv} = \mathbf{d}_r + \mathbf{d}_w$ to the system are superposition forms of random function \mathbf{d}_r and generalized disturbance \mathbf{d}_w (wind, waves, and current action).

The random function \mathbf{d}_r is set such that

$$\begin{cases} d_{rx} = 1.3\sin(0.1\pi t) + 0.3\cos(0.13\pi t) + 0.1k_s\text{rand}(1) \\ d_{ry} = 1.3\cos(0.12\pi t) + 0.3\sin(0.12\pi t) + 0.1k_s\text{rand}(1) \\ d_{rz} = 1.3\sin(0.13\pi t) + 0.3\cos(0.1\pi t) + 0.1k_s\text{rand}(1) \\ d_{r\phi} = 0.3\cos(0.13\pi t) + 0.1k_s\text{rand}(1) \\ d_{r\theta} = 0.3\sin(0.12\pi t) + 0.1k_s\text{rand}(1) \\ d_{r\psi} = 0.3\cos(0.1\pi t) + 0.1k_s\text{rand}(1) \end{cases} \quad (62)$$

The parameter settings for generalized interference \mathbf{d}_w are given in Table A2 in Appendix A.

In addition, on the basis of the new controller designed in this study, two other controllers are designed for a comparative study: one uses the conventional adaptive linear sliding mode control (LSMC) law, and the other uses the conventional PID control law.

The conventional adaptive sliding mode control (ASMC) law is designed as follows:

$$\begin{aligned} \tau_v &= \mathbf{J}^T \mathbf{M}_\eta \mathbf{u} \\ \mathbf{u} &= \ddot{\eta}_d - \mathbf{f} - k_1 \dot{e} - \hat{\mathbf{D}} \text{sign}(\mathbf{s}) - c_3 \mathbf{s} \end{aligned} \quad (63)$$

$$\dot{D}_i = \gamma_1 (|s_i| - \mu_1 \hat{D}_i), i = 1, 2, \dots, 6 \quad (64)$$

Remark 6. The hyperbolic tangent function $\tanh(s_i / \xi_i)$, $\xi_i \in (0, 1)$ is used to substitute the sign function $\text{sign}(s_i)$ in weak chattering. It is worth noting that the smaller the ξ_i value, the closer the properties of the hyperbolic tangent function to the sign function.

The parameters of linear sliding mode control laws (63) and (64) of the controller for the control group are chosen as $k_{1p} = 1.5, k_{1\ominus} = 2.5, c_{3p} = c_{3\ominus} = 1.5$. The adaptive law design parameters for the robust switching term are $\gamma_{1p} = \gamma_{2\ominus} = 2.5, \mu_{1p} = \mu_{1\ominus} = 0.02$.

The conventional PID control law is designed as follows:

$$\begin{aligned} \tau_v &= \mathbf{J}^T \mathbf{M}_\eta \mathbf{u} \\ \mathbf{u} &= -k_p e - k_I \int e dt - k_d \dot{e} \end{aligned} \quad (65)$$

The controller parameters for classical PID control law (65) are selected as $k_{pp} = k_{p\ominus} = 20, k_{Ip} = k_{I\ominus} = 10, k_{dp} = 5, k_{d\ominus} = 10$.

It should be noted that the control parameters of the above controllers were determined using the trial-and-error method to obtain near-optimal control parameters.

4.1. Coaxial HAUV Spiral Upward Cross-Domain Maneuvering Control with the NNAFTSMC

In the following simulation, the main consideration is testing the control effect of the designed adaptive neural network robust controller on the coaxial HAUV take-off crossing the water surface. The initial position of the HAUV is set to $[x_0, y_0, z_0, \dot{x}_0, \dot{y}_0, \dot{z}_0]^T = [0.2, 1.8, -2.1, 0, 0, 0]^T$, and the initial attitude state is set to $[\phi_0, \theta_0, \psi_0, \dot{\phi}_0, \dot{\theta}_0, \dot{\psi}_0]^T = [0, 0, \pi/6, 0, 0, 0]^T$. To further evaluate the performance of the designed NNAFTSMC method, sensor measurement noise effects are added to all states. Gaussian noise is selected as sensor noise, and its characteristics are shown in Figure 6.

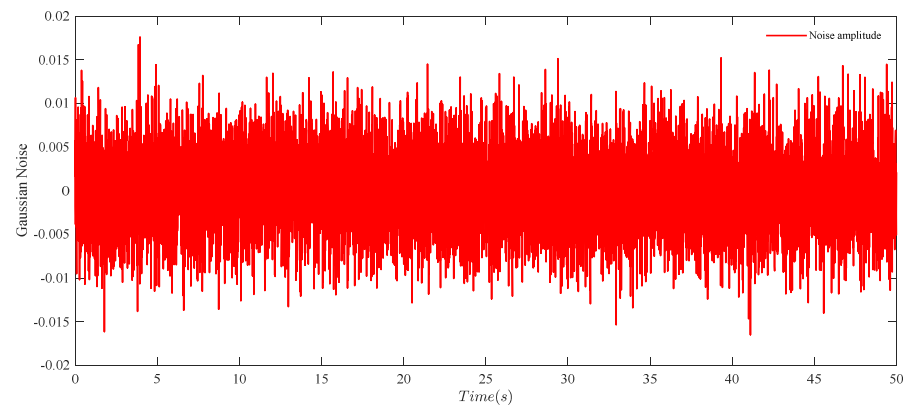


Figure 6. Sensor measurement noises of the coaxial HAUV.

The desired value of the cross-domain maneuvering trajectory selected for leaving water is shown in Equation (66):

$$\begin{cases} x_d = 2\sin(0.1\pi t), (\text{m}) \\ y_d = 2\cos(0.1\pi t), (\text{m}) \\ z_d = 0.1t - 2.0, (\text{m}) \\ \psi_d = 0.01, (\text{rad}) \end{cases} \quad (66)$$

Some simulation results for Case 1 are provided in Figures 7–12. Figures 7 and 8 show the tracking response of the position loop after employing the proposed controller. It can be clearly seen that the proposed composite robust controller performs well, even in the presence of sensor noise. The tracking evolution results of the three channels of the translational motion over time are given in Figure 7, which shows that each channel achieves good tracking results. However, the presence of sensor noise causes obvious fluctuations in the tracking curve near the reference trajectory. Figure 8 demonstrates the 3-D spiral climb effect. The coaxial HAUV trajectory starts from underwater, traverses the wavy water surface, and spirals up into the air, and the whole process demonstrates a good space-tracking effect. Figure 9 shows the attitude-tracking effect of the proposed inner-loop controller. In Figure 9a, it can be observed that the controller can drive the coaxial HAUV to accurately track the desired attitude angle. The desired angle fluctuates due to noise. In addition to the noise superimposed on the state, the jump of the angle tracking is more obvious in Figure 9b. Figure 10 shows the evolution effect of the tracking error of the position and attitude, and it is clear that the error, despite large fluctuations in the initial state, is quickly able to reach the set boundaries and stabilize. However, by comparing Figure 10a,b, it can be seen that the noise causes the control error to jump frequently around 0. Figure 11 illustrates the online approximation results of the employed RBFNN for the unknown nonlinear function against the setup value. Figure 12 shows the norm of the error between the observed result and the value of the unknown nonlinear function set using the RBFNN. By combining the results of Figures 11 and 12, it can be seen that, despite the large discrepancy between the initial value of the neural network approximator and the total uncertainty, the neural network is still able to obtain accurate approximations quickly, and the above shows that the proposed neural network approximator can provide reliable uncertainty function estimates for controller design. Noise deteriorates the results of the RBFNN's online identification of nonlinear functions, and the reconstruction ability or accuracy of the neural network decreases.

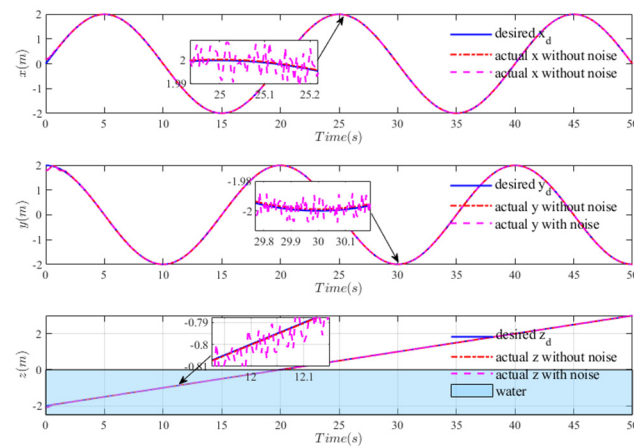


Figure 7. Tracking results of the coaxial HAUV in x, y, and z channels for Case 1.

Figure 13 shows the evolution of the adaptive law parameters of the designed controller’s robust switching terms over time. It can be seen that the reconstruction ability of the neural network decreases and that the adaptive parameters become larger to enhance the robustness of the controller. The adaptive law and the RBFNN approximator complement each other and enhance the robustness of the system. Figure 14 shows the evolution of the norm of the weight coefficients under each degree of freedom of the designed RBFNN approximator over time. It is worth noting that noise seems to have a weak effect on the weight coefficient results over time, and the values of the weight coefficient norm are similar. If the exact state quantity can be obtained, the RBFNN will achieve more accurate online identification and reduce the dependence on model parameters in the subsequent stages. Figure 15 shows the variation in the control signal. During the 50 s simulation, in the initial stage, the coaxial HAUV receives buoyancy compensation, and the lift output is small; in the later stage, the coaxial HAUV enters the air from the water, the buoyancy disappears, and the total lift has to overcome the effect of gravity, so the output value becomes larger. Sensor noise makes the state variable fluctuate at a high frequency, which further causes the controller’s solution results to fluctuate. This is very bad for the actuator. This is why real flight controllers need to incorporate various efficient filtering algorithms to avoid the effect of noise on the control signal.

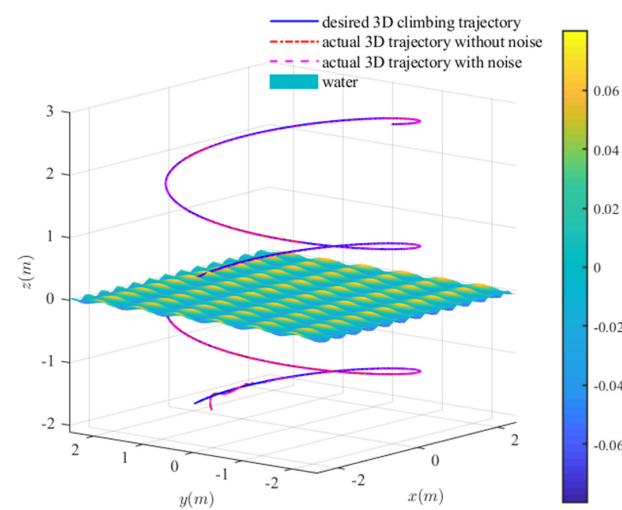
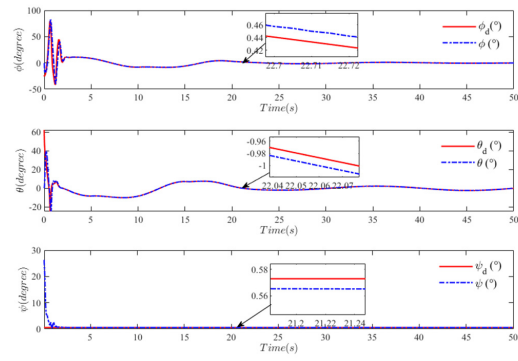
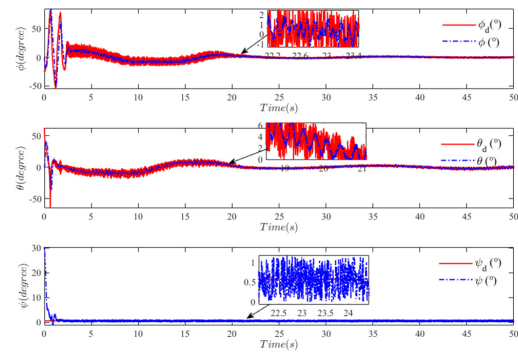


Figure 8. The 3D view position tracking results in Case 1.

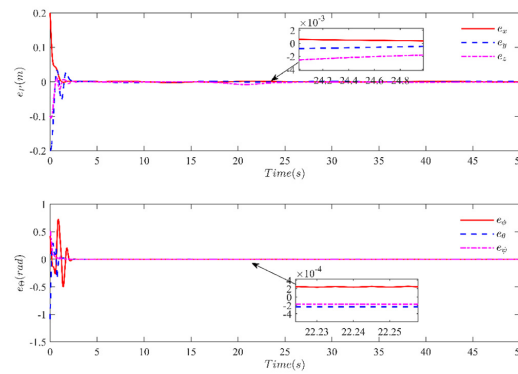


(a) Sensor noise absence

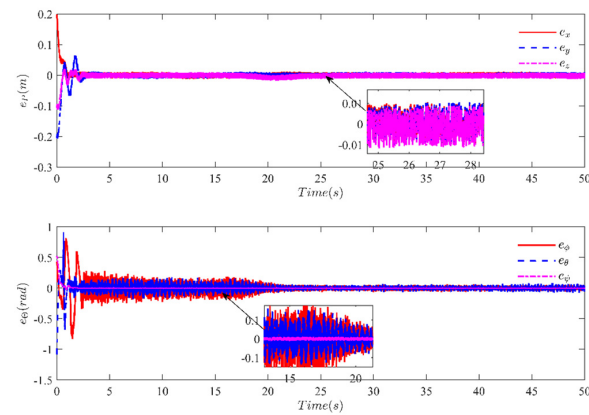


(b) Sensor noise presence

Figure 9. Attitude angle tracking results in Case 1.



(a) Sensor noise absence



(b) Sensor noise presence

Figure 10. Attitude angle tracking error evolutionary results in Case 1.

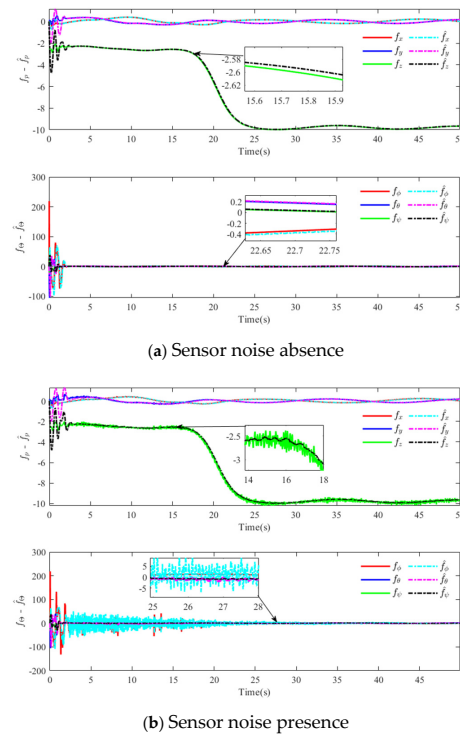


Figure 11. Attitude angle tracking results in Case 1.

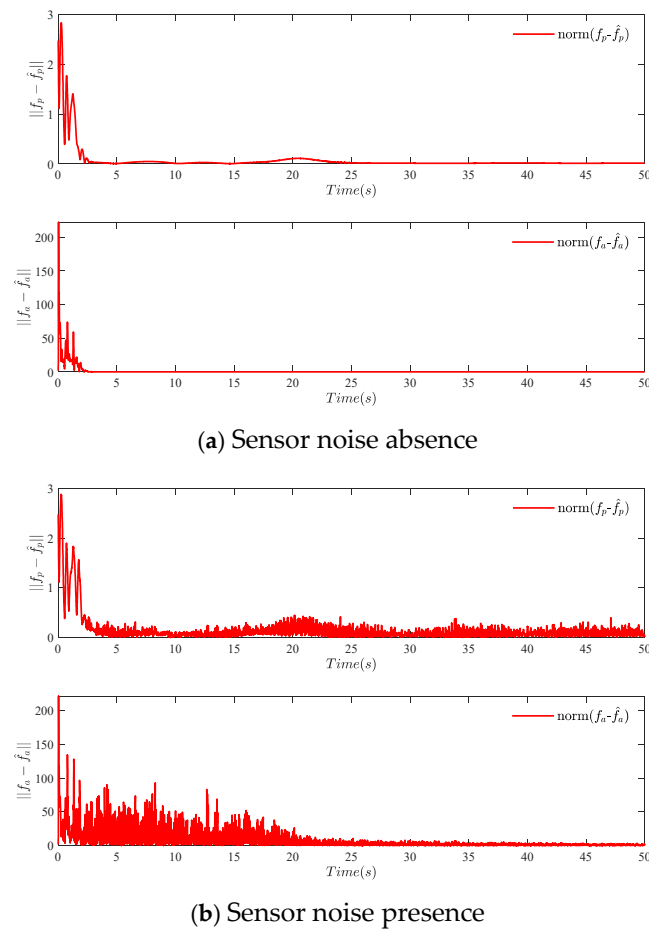


Figure 12. Identification of evolution of nonlinear functions of RBFNN in position and attitude loops in Case 1.

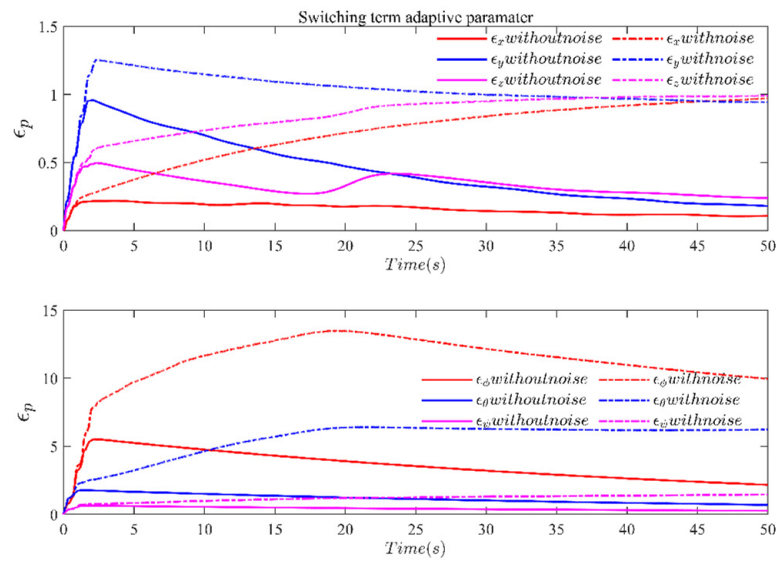


Figure 13. Evolution of the designed controller robust switching terms in Case 1.

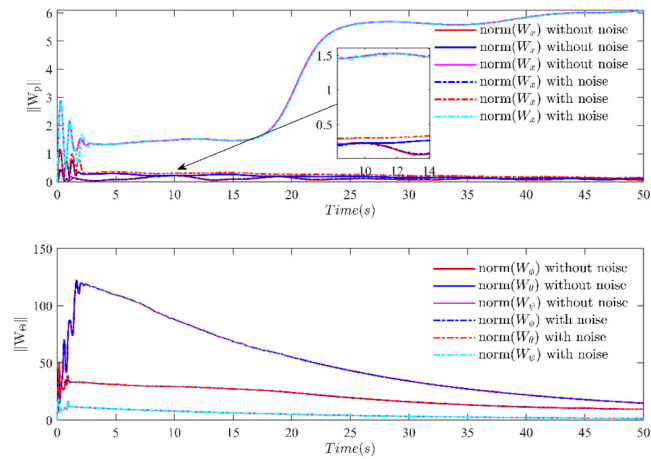
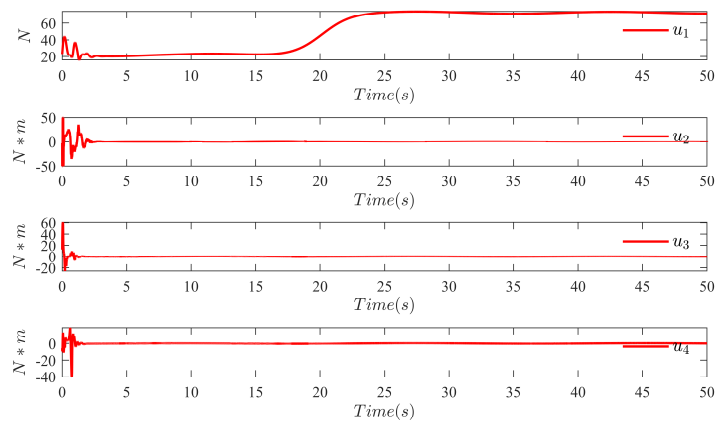
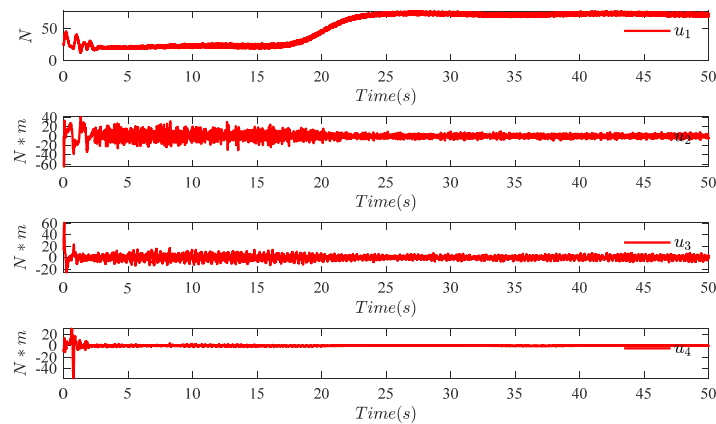


Figure 14. RBFNN norm evolution results of weight coefficient estimates for each DOF.



(a) Sensor noise absence

Figure 15. Cont.



(b) Sensor noise presence

Figure 15. Variation in the control signal in Case 1.

4.2. Comparative Simulation of Control Effects of Different Control Algorithms

In the following simulations, the main aim is to test the control effectiveness of the designed NNAFTSMC and the conventional ASMC and PID controller in achieving the cross-domain process of the coaxial HAUV. The controller parameters and the initial position of the coaxial HAUV are stated in the previous section. As the main purpose is to test the effects of different controllers, noise is not considered in this section.

For a quantitative comparative analysis, the tracking performance of the three controllers involved in this study can be quantitatively analyzed using the mean absolute error (MAE) and root mean square error (RMSE). The MAE and RMSE are defined in the following equations:

$$\begin{aligned} \text{MAE} &= \frac{1}{n} \sum_{i=1}^n |e| \\ \text{RMSE} &= \sqrt{\frac{1}{n} \sum_{i=1}^n e^2} \end{aligned} \quad (67)$$

where e is the amount of error, thus denoting the number of discrete errors in the control evolution process. RMSE vs. MAE: The RMSE is equivalent to the L2 paradigm, and the MAE is equivalent to the L1 paradigm. The higher the number, the more the calculation is related to larger discrete values and ignores smaller values, which is why the RMSE is more sensitive to outliers (i.e., if there is a predicted value that is very different from the true value, then the RMSE will be large).

Some simulation results of the three different controllers are given in Figures 16–23 to further illustrate the superiority of the designed adaptive neural network sliding mode controller through the control effects of the different controllers. Figures 16–19 show the tracking response results of the position and attitude loops obtained using the three controllers. It can be seen that the three controllers used are capable of realizing the trans-media trajectory tracking process of the coaxial HAUV. This further validates the results of previous scholars who achieved trans-domain motion through PID control algorithms and ASMC algorithms. However, the tracking effect achieved by the PID controllers is found to deviate the furthest from the preset trajectory, as shown in the comparative tests and results in Figures 16–19, demonstrating the limitations of classical PID controllers in facing the control problem under such time-varying parameters and multivariate disturbance conditions. Figures 20 and 21 show the evolutionary effect of the tracking error on position and attitude; it is clear that the adaptive neural network sliding mode controller (NNASMC) achieves the best steady state for the control error and that its convergence speed is superior to that of the ASMC. The upper limit of the final settling time of the NNASMC is 4.97 s, which is consistent with the actual stabilizing effect of the control error. The results show

that the controller designed in this study achieves the fastest convergence speed. The MAE data in Table 1 show that the NNASMC obtained the smallest MAE parameter in each degree of freedom, which means that the designed controller has the best performance in terms of stabilizing the control error to zero. However, the NNASMC is rather less effective than the ASMC in terms of RMSE data performance for the roll and pitch channels. The reason for this phenomenon is that the underdriven peculiarity of the coaxial HAUV causes the pitch and roll angles to originate from the virtual control signals of the position loop, and the fluctuating process of the RBFNN approximator’s approximation in the initial stage leads to more fluctuations in the desired attitude angle, which further causes fluctuations in the control error. As the introduction of the RBFNN approximator relaxes the requirement of accurate data for the model parameters of the complex hydrodynamic process, and the fluctuation phenomenon disappears rapidly as the approximator rapidly approximates the unknown nonlinear function in the model, the above phenomenon is within the acceptable range.

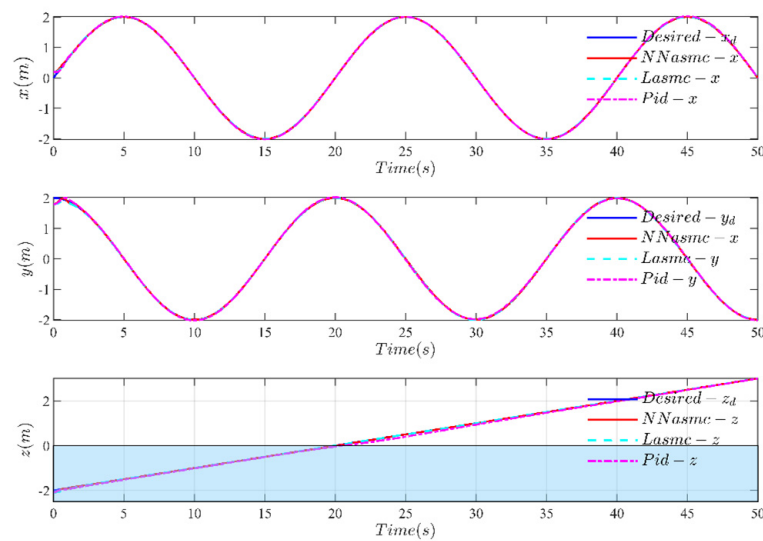


Figure 16. Tracking results of position channels with different controllers.

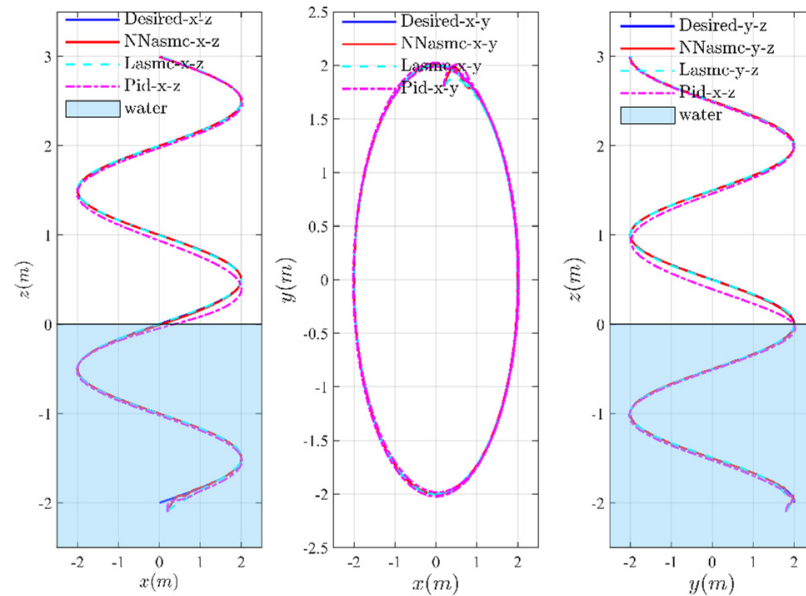


Figure 17. Tracking results for the 2D plane with different controllers.

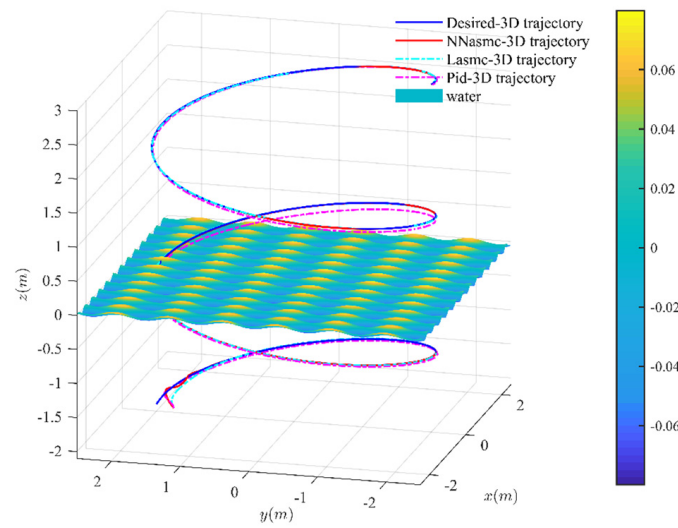


Figure 18. The 3-D trajectory tracking results with different controllers.

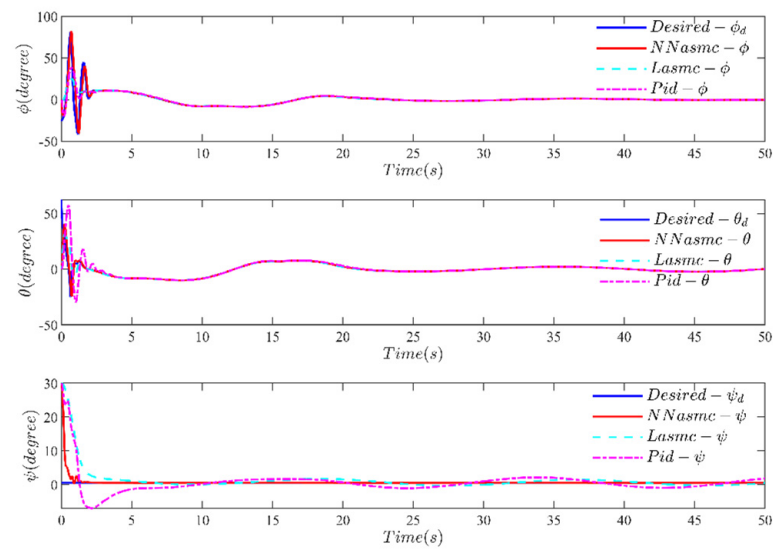


Figure 19. Attitude angle tracking results with different controllers.

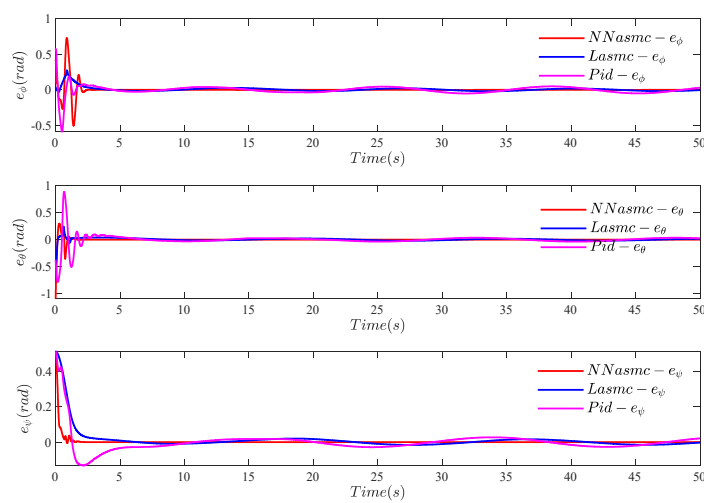


Figure 20. Evolution of attitude angle tracking error with different controllers.

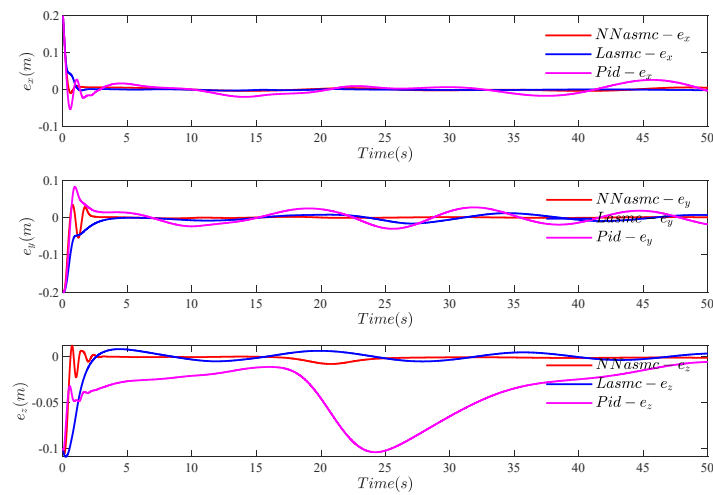


Figure 21. Evolution of position tracking error with different controllers.

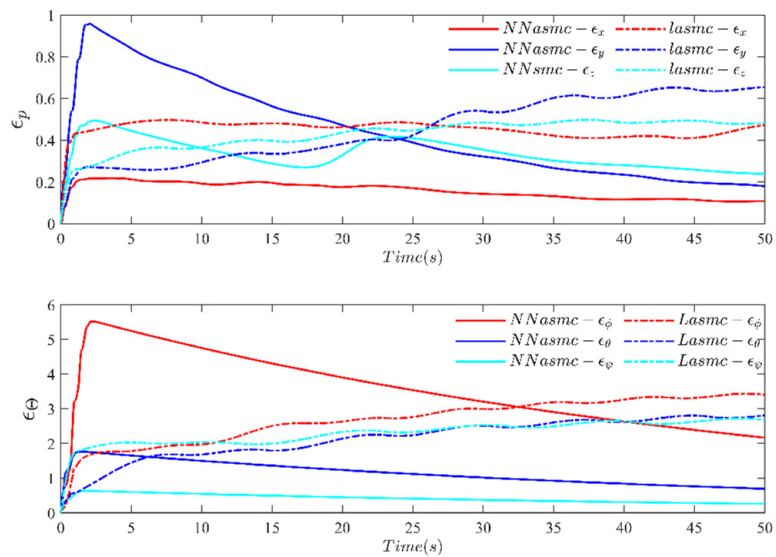


Figure 22. Adaptive parameter evolution results of NNAsmc and traditional ASMC.

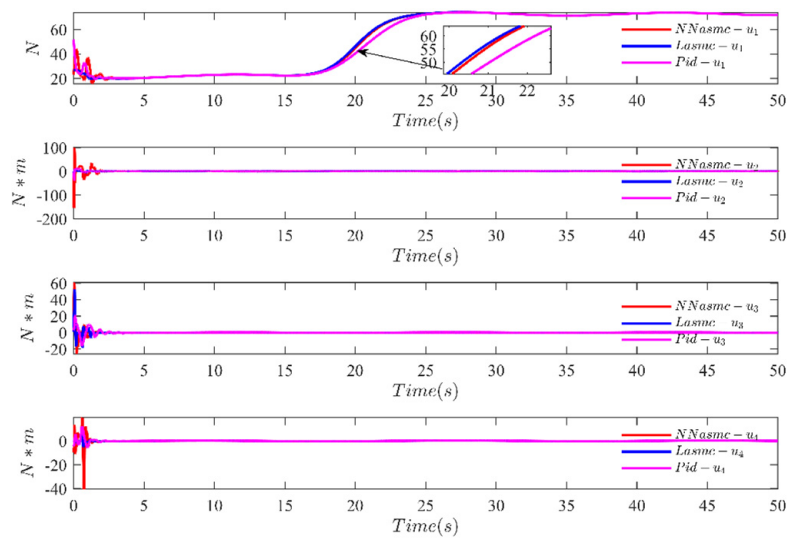


Figure 23. Results of the evolution of the control inputs for the different controllers.

Table 1. Performance in comparative simulations.

(ITEM TYPE)	x_e	y_e	z_e	ϕ_e	θ_e	ψ_e	TOTAL
MAE (NNAFTSMC)	0.0020	0.0030	0.0024	0.0108	0.0048	0.0026	0.0256
MAE (ASMC)	0.0034	0.0092	0.0057	0.0174	0.0159	0.0200	0.0717
MAE (PID)	0.0110	0.0168	0.0376	0.0345	0.0394	0.0288	0.1680
RMSE (NNAFTSMC)	0.0107	0.0157	0.008	0.0650	0.0415	0.0269	0.0295
RMSE (ASMC)	0.0102	0.0210	0.0149	0.0307	0.0274	0.0613	0.0392
RMSE (PID)	0.0157	0.0242	0.0467	0.0699	0.0984	0.0609	0.0776

Figure 22 shows the evolution of the switching term adaptive law parameter over time for the NNASMC and ASMC. It can be seen that the switching term adaptive parameter first increases and then converges to a bounded constant, but the adaptive parameter of the NNASMC is larger than that of the ASMC. The main reason for this phenomenon is that the RBFNN approximator does not achieve an accurate approximation of the model's nonlinear function in the initial stage, which results in the robustness of the whole system being borne by the switching term; however, after the approximator achieves effective online identification, the switching term parameter of the NNASMC decays fast and is smaller than the switching term adaptive law parameter of the ASMC, which indeed attenuates the jitter effect effectively. The evolution results of the different controllers in solving the control inputs are shown in Figure 23. The evolution trends of the control inputs solved using the different controllers are similar; however, the designed NNASMC achieves the most accurate control signal in terms of the control effect.

5. Conclusions and Outlook

In this study, the discrete dynamics model of a coaxial HAUV is combined with a relatively accurate continuous dynamic model based on smooth switching coefficients. The resulting model unifies the description of three states, namely, air flight, underwater motion, and trans-media, and the smooth and continuous switching coefficients prevent abrupt model changes. In order to solve the coaxial HAUV trans-media motion control problem with complex marine environment disturbances and model uncertainties, an adaptive fixed-time sliding mode controller based on the RBFNN approximation strategy is designed. The system convergence time of this controller does not depend on the initial state, and it can achieve error convergence in a fixed time, thus realizing the fast trans-domain high-precision motion of the coaxial HAUV. The nonlinear function is approximated online using the RBFNN; thus, the priori upper bound of the total uncertainty is not considered. At the same time, the estimation error of the neural network is eliminated by combining the adaptive law, which further enhances the robustness of the control system. The influence of sensor noise on the controller effect is tested in simulations. The simulation results show that the designed controller can realize cross-domain tracking error control under the influence of noise. However, noise decreases the identification ability of the RBFNN and causes the control error to fluctuate significantly. Through a quantitative analysis of the MAE and RMSE, the effectiveness and superiority of the proposed scheme in dealing with the cross-domain control problem of coaxial HAUVs are verified in comparison with the traditional PID control algorithm and ASMC algorithm.

Although the above work is limited to theoretical modeling analyses and controller design at this stage and the testing of the designed controllers on actual prototypes has not yet been carried out, it serves as a reference for the development of HAUVs and the design of the same type of HAUV controllers. In future work, the design and manufacture of a prototype will be completed as soon as possible, and experimental methods will be used to test the reliability of the controller in real application scenarios. In order to achieve the safety of cross-domain flight in complex sea states, more complex input constraints will be considered, such as efficiency loss, input saturation, and status filtering. In addition, the control input quantization mechanism is also an interesting research topic.

Author Contributions: Conceptualization, M.L., W.Y., S.W. and Z.X.; methodology, M.L. and F.L.; software, M.L., F.L. and S.W.; validation, W.Y., F.L., Z.X., Y.S. and W.W.; formal analysis, F.L. and S.W.; writing—review and editing, W.Y., Z.X., F.L. and W.W.; visualization, M.L., W.Y. and Z.X.; supervision, Y.S. and W.W.; resources, Y.S. and W.W. All authors have read and agreed to the published version of the manuscript.

Funding: This research was funded by the Feng Lei Youth Innovation Fund of CARDC (grant/award numbers FL018070012 and ZZZH2000907098), the National Defense Key Laboratory Fund (grant/award number 614222003061709), and the Key Laboratory of Cross-Domain Flight Interdisciplinary Technology Fund (grant/award number 2024-ZY0301).

Data Availability Statement: The parameters used in the simulation are given in the paper or appendix. If any researchers need to obtain more in-depth technical details of this study or want to engage in academic communication, please contact us.

Acknowledgments: The authors are very grateful for the support of the Cross-media Vehicle Research Center of the China Aerodynamics Research and Development Center and the Science and Technology on Underwater Vehicle Laboratory of Harbin Engineering University.

Conflicts of Interest: The authors declare no conflicts of interest.

Appendix A

Table A1. Model system parameters applied in simulation.

Parameter Symbol	Numerical Value	Parameter Symbol	Numerical Value
m/kg	7.4	$X_{u u}, X_{u u a}/N \cdot (\text{m/s})^{-2}$	−8.82, −0.001
$I_x/\text{kg} \cdot \text{m}^2$	0.232	$Y_{v v}, Y_{v v a}/N \cdot (\text{m/s})^{-2}$	−8.82, −0.001
$I_y/\text{kg} \cdot \text{m}^2$	0.232	$Z_{w w}, Z_{w w a}/N \cdot (\text{m/s})^{-2}$	−4.73, −0.0005
$I_z/\text{kg} \cdot \text{m}^2$	0.342	$K_{p p}, K_{p p a}/N \cdot (\text{m/s})^{-2}$	−0.62, −0.0006
$X_{\dot{u}}/\text{kg}$	−2.24	$M_{q q}, M_{q q a}/N \cdot (\text{m/s})^{-2}$	−0.62, −0.0006
$Y_{\dot{v}}/\text{kg}$	−2.24	$N_{r r}, N_{r r a}/N \cdot (\text{m/s})^{-2}$	−0.32, −0.0003
$Z_{\dot{w}}/\text{kg}$	−1.24	$R, H/\text{m}$	0.06, 0.5
$K_{\dot{p}}/\text{kg} \cdot \text{m}^2$	−0.083	r_B/m	(0, 0, 0.05)
$M_{\dot{q}}/\text{kg} \cdot \text{m}^2$	−0.083	$\rho_w/\text{kg} \cdot \text{m}^{-3}$	1025
$N_{\dot{r}}/\text{kg} \cdot \text{m}^2$	−0.051		

Table A2. Wind, wave, and current parameters applied in the simulation.

Parameter	Numerical Value	Parameter	Numerical Value
A_{x1}/m	0.001	A_{y1}/m	0.07
A_{x2}/m	1	A_{y2}/m	0.04
$\omega_{x1}/\text{rad} \cdot \text{s}^{-1}$	1	φ_{x1}/rad	0
$\omega_{x2}/\text{rad} \cdot \text{s}^{-1}$	10	φ_{x2}/rad	0
$\omega_{y1}/\text{rad} \cdot \text{s}^{-1}$	2	φ_{y1}/rad	0
$\omega_{y2}/\text{rad} \cdot \text{s}^{-1}$	7	φ_{y2}/rad	0
$C_{d\dot{w}}/N \cdot (\text{m/s})^{-2}$	0.1	C_m	0.8
$C_{d\dot{c}}/N \cdot (\text{m/s})^{-2}$	0.03	C_D	0.8
$v_w/\text{m} \cdot \text{s}^{-1}$	(0.1, 0.1, 0)	$v_c/\text{m} \cdot \text{s}^{-1}$	(−0.5, −0.5, 0)

References

- Murphy, R.R.; Steimle, E.; Griffin, C.; Cullins, C.; Hall, M.; Pratt, K. Cooperative use of unmanned sea surface and micro aerial vehicles at Hurricane Wilma. *J. Field Robot.* **2008**, *25*, 164–180. [[CrossRef](#)]
- Wang, Y.; Zhang, M.; Wilson, P.A.; Liu, X. Adaptive neural network-based backstepping fault tolerant control for underwater vehicles with thruster fault. *Ocean Eng.* **2015**, *110*, 15–24. [[CrossRef](#)]

3. Zhang, E.; Li, J.; Zhu, C.; Huang, B. Bearing-based prescribed-time formation control of underactuated autonomous surface vehicles with the interception of attackers. *Ocean Eng.* **2022**, *262*, 112187. [CrossRef]
4. Nugroho, A.T.; Jaya, I.; Naulita, Y. Development and Field Test of Gps-Gsm Drifting Buoy for Measurement of Sea Surface Current Data. *J. Appl. Geospat. Inf.* **2022**, *6*, 607–614. [CrossRef]
5. Hisaki, Y. Validation of Drifting Buoy Data for Ocean Wave Observation. *J. Mar. Sci. Eng.* **2021**, *9*, 729. [CrossRef]
6. Sun, Y.; Liu, X.; Cao, K.; Shen, H.; Li, Q.; Chen, G.; Xu, J.; Ji, A. Design and Theoretical Research on Aerial-Aquatic Vehicles: A Review. *J. Bionic Eng.* **2023**, *20*, 2512–2541. [CrossRef]
7. Wang, X.; Yang, X.; Zhao, J.; Pei, X.; Su, H.; Wang, T.; Hou, T. Aquatic unmanned aerial vehicles (AquaUAV): Bionic prototypes, key technologies, analysis methods, and potential solutions. *Sci. China Technol. Sci.* **2023**, *66*, 2308–2331. [CrossRef]
8. Zeng, Z.; Lyu, C.; Bi, Y.; Jin, Y.; Lu, D.; Lian, L. Review of hybrid aerial underwater vehicle: Cross-domain mobility and transitions control. *Ocean Eng.* **2022**, *248*, 110840. [CrossRef]
9. Yao, G.; Li, Y.; Zhang, H.; Jiang, Y.; Wang, T.; Sun, F.; Yang, X. Review of hybrid aquatic-aerial vehicle (HAUV): Classifications, current status, applications, challenges and technology perspectives. *Prog. Aerosp. Sci.* **2023**, *139*, 100902. [CrossRef]
10. Verne, J. *The Master of the World; Read How You Want*, Hybrid Publishers: Melbourne, Australia, 2008.
11. Yang, X.; Wang, T.; Liang, J.; Yao, G.; Liu, M. Survey on the novel hybrid aquatic–aerial amphibious aircraft: Aquatic unmanned aerial vehicle (AquaUAV). *Prog. Aerosp. Sci.* **2015**, *74*, 131–151. [CrossRef]
12. Petrov, G. Flying submarine. *J. Fleet* **1995**, *3*, 52–53. Available online: http://www.airforce.ru/aircraft/miscellaneous/flying_submarine/index.htm (accessed on 17 December 2013).
13. Reid, B.D. *The Flying Submarine: The Story of the Invention of the Reid Flying Submarine, RFS-1*; Heritage Books: Berwyn Heights, MD, USA, 2012.
14. U.C.V.C. Convair. *Convair Flying Submarine Report (Convair Report HP-62-016)*; U.C.V.C.: San Diego, CA, USA, 1962.
15. Zimmerman, S.; Abdelkefi, A. Review of marine animals and bioinspired robotic vehicles: Classifications and characteristics. *Prog. Aerosp. Sci.* **2017**, *93*, 95–119. [CrossRef]
16. Siddall, R.; Ortega Ancel, A.; Kovač, M. Wind and water tunnel testing of a morphing aquatic micro air vehicle. *Interface Focus* **2017**, *7*, 20160085. [CrossRef] [PubMed]
17. Zufferey, R.; Ancel, A.O.; Farinha, A.; Siddall, R.; Armanini, S.F.; Nasr, M.; Brahmali, R.V.; Kennedy, G.; Kovac, M. Consecutive aquatic jump-gliding with water-reactive fuel. *Sci. Robot.* **2019**, *4*, eaax7330. [CrossRef] [PubMed]
18. Farinha, A.; Di Tria, J.; Zufferey, R.; Armanini, S.F.; Kovac, M. Challenges in Control and Autonomy of Unmanned Aerial-Aquatic Vehicles. In Proceedings of the 29th Mediterranean Conference on Control and Automation (MED), Puglia, Italy, 22–25 June 2021; pp. 937–942.
19. Zhou, X.; Zhong, H.; Zhang, H.; He, W.; Hua, H.; Wang, Y. Current Status, Challenges, and Prospects for New Types of Aerial Robots. *Engineering* **2024**, *41*, 19–34. [CrossRef]
20. Wei, J.; Sha, Y.-B.; Hu, X.-Y.; Cao, Z.; Chen, D.-P.; Zhou, D.; Chen, Y.-L. Research on Aerodynamic Characteristics of Trans-Media Vehicles Entering and Exiting the Water in Still Water and Wave Environments. *Drones* **2023**, *7*, 69. [CrossRef]
21. Drews, P.L.; Neto, A.A.; Campos, M.F. Hybrid unmanned aerial underwater vehicle: Modeling and simulation. In Proceedings of the 2014 IEEE/RJS International Conference on Intelligent Robots and Systems, Chicago, IL, USA, 14–18 September 2014; pp. 4637–4642.
22. Pinheiro, P.M.; Neto, A.A.; Grando, R.B.; da Silva, C.B.; Aoki, V.M.; Cardoso, D.S.; Horn, A.C.; Drews, P.L.J. Trajectory Planning for Hybrid Unmanned Aerial Underwater Vehicles with Smooth Media Transition. *J. Intell. Robot. Syst.* **2022**, *104*, 1–16. [CrossRef]
23. Alzu'Bi, H.; Mansour, I.; Rawashdeh, O. Loon Copter: Implementation of a hybrid unmanned aquatic–aerial quadcopter with active buoyancy control. *J. Field Robot.* **2018**, *35*, 764–778. [CrossRef]
24. Mercado, D.; Maia, M.; Díez, F.J. Aerial-underwater systems, a new paradigm in unmanned vehicles. *J. Intell. Robot. Syst.* **2019**, *95*, 229–238. [CrossRef]
25. Tan, L.; Liang, S.; Su, H.; Qin, Z.; Li, L.; Huo, J. Research on Amphibious Multi-Rotor UAV Out-of-Water Control Based on ADRC. *Appl. Sci.* **2023**, *13*, 4900. [CrossRef]
26. Chen, Q.; Zhu, D.; Liu, Z. Attitude control of aerial and underwater vehicles using single-input FUZZY P+ID controller. *Appl. Ocean Res.* **2020**, *107*, 102460. [CrossRef]
27. Zongcheng, M.; Xianyong, J.; Zhuoran, Z.; Shuchen, X.; Tian, Z.; Guoshuai, L. GA and RBFNN based PID for altitude-depth control of the multirotor Hybrid Aerial Underwater Vehicles. *J. Phys. Conf. Ser.* **2022**, *2239*, 012005. [CrossRef]
28. Gambhire, S.J.; Kishore, D.R.; Londhe, P.S.; Pawar, S.N. Review of sliding mode based control techniques for control system applications. *Int. J. Dyn. Control* **2020**, *9*, 363–378. [CrossRef]
29. Chen, Y.; Liu, Y.; Meng, Y.; Yu, S.; Zhuang, Y. System Modeling and Simulation of an Unmanned Aerial Underwater Vehicle. *J. Mar. Sci. Eng.* **2019**, *7*, 444. [CrossRef]
30. Ma, Z.; Feng, J.; Yang, J. Research on vertical air–water trans-media control of Hybrid Unmanned Aerial Underwater Vehicles based on adaptive sliding mode dynamical surface control. *Int. J. Adv. Robot. Syst.* **2018**, *15*, 1729881418770531. [CrossRef]
31. Bi, Y.; Lu, D.; Zeng, Z.; Lian, L. Dynamics and control of hybrid aerial underwater vehicle subject to disturbances. *Ocean Eng.* **2022**, *250*, 110933. [CrossRef]
32. Lu, M.; Liao, F.; Xing, B.; Fan, Z.; Su, Y.; Wu, W. Adaptive Finite-Time Trajectory Tracking Control for Coaxial HAUVs Facing Uncertainties and Unknown Environmental Disturbances. *Appl. Sci.* **2023**, *13*, 8026. [CrossRef]

33. Lu, D.; Xiong, C.; Zeng, Z.; Lian, L. Adaptive dynamic surface control for a hybrid aerial underwater vehicle with parametric dynamics and uncertainties. *IEEE J. Ocean. Eng.* **2019**, *45*, 740–758. [[CrossRef](#)]
34. Lu, D.; Guo, Y.; Xiong, C.; Zeng, Z.; Lian, L. Takeoff and Landing Control of a Hybrid Aerial Underwater Vehicle on Disturbed Water's Surface. *IEEE J. Ocean. Eng.* **2021**, *47*, 295–311. [[CrossRef](#)]
35. Chen, G.; Liu, A.; Hu, J.; Feng, J.; Ma, Z. Attitude and Altitude Control of Unmanned Aerial-Underwater Vehicle Based on Incremental Nonlinear Dynamic Inversion. *IEEE Access* **2020**, *8*, 156129–156138. [[CrossRef](#)]
36. Zhang, H.; Zeng, Z.; Yu, C.; Jiang, Z.; Han, B.; Lian, L. Predictive and sliding mode cascade control for cross-domain locomotion of a coaxial aerial under-water vehicle with disturbances. *Appl. Ocean. Res.* **2020**, *100*, 102183. [[CrossRef](#)]
37. Wu, S.; Xie, L.; Xian, J.; Liao, F.; Wu, W.; Lu, M.; Yi, X. Reinforcement learning-based finite-time cross-media tracking control for a cross-media vehicle under unknown dynamics and disturbances. *IET Control Theory Appl.* **2024**, *18*, 1475–1490. [[CrossRef](#)]
38. Polyakov, A. Nonlinear Feedback Design for Fixed-Time Stabilization of Linear Control Systems. *IEEE Trans. Autom. Control* **2011**, *57*, 2106–2110. [[CrossRef](#)]
39. Wang, Z.; Su, Y.; Zhang, L. Fixed-time attitude tracking control for rigid spacecraft. *IET Control Theory Appl.* **2020**, *14*, 790–799. [[CrossRef](#)]
40. Yu, L.; He, G.; Wang, X.; Zhao, S. Robust Fixed-Time Sliding Mode Attitude Control of Tilt Trirotor UAV in Helicopter Mode. *IEEE Trans. Ind. Electron.* **2021**, *69*, 10322–10332. [[CrossRef](#)]
41. Huang, Y.J.; Kuo, T.C.; Chang, S.H. Adaptive sliding-mode control for nonlinear systems with uncertain parameters. *IEEE Trans. Syst. Man Cybern. Part B* **2008**, *38*, 534–539. [[CrossRef](#)]
42. Yao, Q. Neural adaptive learning synchronization of second-order uncertain chaotic systems with prescribed performance guarantees. *Chaos Solitons Fractals* **2021**, *152*, 111434. [[CrossRef](#)]
43. Huang, S.; Yang, Y. Adaptive Neural-Network-Based Nonsingular Fast Terminal Sliding Mode Control for a Quadrotor with Dynamic Uncertainty. *Drones* **2022**, *6*, 206. [[CrossRef](#)]
44. Wang, J.; Wang, P.; Tian, B. Hyperbolic tangent function-based fixed-time event-triggered control for quadrotor aircraft with prescribed performance. *J. Frankl. Inst.* **2022**, *359*, 6267–6285. [[CrossRef](#)]
45. Ma, J.; Ge, S.S.; Zheng, Z.; Hu, D. Adaptive NN Control of a Class of Nonlinear Systems with Asymmetric Saturation Actuators. *IEEE Trans. Neural Networks Learn. Syst.* **2014**, *26*, 1532–1538. [[CrossRef](#)]
46. Chen, Q.; Xie, S.; Sun, M.; He, X. Adaptive Nonsingular Fixed-Time Attitude Stabilization of Uncertain Spacecraft. *IEEE Trans. Aerosp. Electron. Syst.* **2018**, *54*, 2937–2950. [[CrossRef](#)]
47. Alsaade, F.W.; Yao, Q.; Al-Zahrani, M.S.; Alzahrani, A.S.; Jahanshahi, H. Neural-based fixed-time attitude tracking control for space vehicle subject to constrained outputs. *Adv. Space Res.* **2022**, *71*, 3588–3599. [[CrossRef](#)]
48. Zhou, B.; Huang, B.; Su, Y.; Zheng, Y.; Zheng, S. Fixed-time neural network trajectory tracking control for underactuated surface vessels. *Ocean Eng.* **2021**, *236*, 109416. [[CrossRef](#)]
49. Zhao, Z.; Jin, X. Adaptive neural network-based sliding mode tracking control for agricultural quadrotor with variable payload. *Comput. Electr. Eng.* **2022**, *103*, 108336. [[CrossRef](#)]
50. Zhu, C.; Huang, B.; Zhou, B.; Su, Y.; Zhang, E. Adaptive model-parameter-free fault-tolerant trajectory tracking control for autonomous underwater vehicles. *ISA Trans.* **2021**, *114*, 57–71. [[CrossRef](#)]
51. Wei, T.; Li, J.; Zeng, Z.; Lian, L. Trans-media resistance investigation of hybrid aerial underwater vehicle base on hydrodynamic experiments and machine learning. *Ocean Eng.* **2022**, *266*, 112808. [[CrossRef](#)]
52. Glida, H.E.; Sentouh, C.; Rath, J.J. Optimal Model-Free Finite-Time Control Based on Terminal Sliding Mode for a Coaxial Rotor. *Drones* **2023**, *7*, 706. [[CrossRef](#)]
53. Zhang, L.; Zheng, Y.; Huang, B.; Su, Y. Finite-time trajectory tracking control for under-actuated unmanned surface vessels with saturation constraint. *Ocean Eng.* **2022**, *249*, 110745. [[CrossRef](#)]
54. Glida, H.E.; Chelih, A.; Abdou, L.; Sentouh, C.; Perozzi, G. Trajectory tracking control of a coaxial rotor drone: Time-delay estimation-based optimal model-free fuzzy logic approach. *ISA Trans.* **2022**, *137*, 236–247. [[CrossRef](#)]
55. Chen, Z.; Yang, X.; Liu, X. RBFNN-based nonsingular fast terminal sliding mode control for robotic manipulators including actuator dynamics. *Neurocomputing* **2019**, *362*, 72–82. [[CrossRef](#)]

Disclaimer/Publisher's Note: The statements, opinions and data contained in all publications are solely those of the individual author(s) and contributor(s) and not of MDPI and/or the editor(s). MDPI and/or the editor(s) disclaim responsibility for any injury to people or property resulting from any ideas, methods, instructions or products referred to in the content.